Astronomy
&
Astrophysics

The relativistic solar particle event on 28 October 2021: Evidence of particle acceleration within and escape from the solar corona[⋆]

Karl-Ludwig Klein[1,2], Sophie Musset[1,3], Nicole Vilmer[1,2], Carine Briand[1,2], Säm Krucker[4,5], Andrea Francesco Battaglia[4,6], Nina Dresing[7], Christian Palmroos[7], and Dale E. Gary[8]

[1] Observatoire de Paris, LESIA, Univ. PSL, CNRS, Sorbonne Univ., Univ. Paris Cité, 5 place Jules Janssen, 92190 Meudon, France
e-mail: ludwig.klein@obspm.fr
[2] Observatoire de Paris, Station de radioastronomie de Nançay, Univ. PSL, CNRS, Univ. d'Orléans, 5 place Jules Janssen, 92190 Meudon, France
[3] European Space Agency (ESA), European Space Research and Technology Centre (ESTEC), Keplerlaan 1, 2201, AZ Noordwijk, The Netherlands
e-mail: sophie.musset@esa.int
[4] University of Applied Sciences and Arts Northwestern Switzerland, Bahnhofstrasse 6, 5210 Windisch, Switzerland
[5] Space Sciences Laboratory, University of California, 7 Gauss Way, 94720 Berkeley, USA
e-mail: krucker@berkeley.edu
[6] ETH Zürich, Rämistrasse 101, 8092 Zürich, Switzerland
[7] Department of Physics and Astronomy, University of Turku, Turku, Finland
[8] Center for Solar-Terrestrial Research, New Jersey Institute of Technology, 323 M L King Jr Boulevard, Newark, NJ 07102-1982, USA

Received 29 April 2022 / Accepted 17 May 2022

ABSTRACT

Aims. We analyse particle, radio, and X-ray observations during the first relativistic proton event of solar cycle 25 detected on Earth. The aim is to gain insight into the relationship between relativistic solar particles detected in space and the processes of acceleration and propagation in solar eruptive events.

Methods. To this end, we used ground-based neutron monitor measurements of relativistic nucleons and space-borne measurements of electrons with similar speed to determine the arrival times of the first particles at 1 AU and to infer their solar release times. We compared the release times with the time histories of non-thermal electrons in the solar atmosphere and their escape to interplanetary space, as traced by radio spectra and X-ray light curves and images.

Results. Non-thermal electrons in the corona are found to be accelerated in different regions. Some are confined in closed magnetic structures expanding during the course of the event. Three episodes of electron escape to the interplanetary space are revealed by groups of decametric-to-kilometric type III bursts. The first group appears on the low-frequency side of a type II burst produced by a coronal shock wave. The two latter groups are accompanied at higher frequencies by bursts with rapid drifts to both lower and higher frequencies (forward- or reverse-drifting bursts). They are produced by electron beams that propagate both sunward and anti-sunward. The first relativistic electrons and nucleons observed near Earth are released with the third group of type III bursts, more than ten minutes after the first signatures of non-thermal electrons and of the formation of the shock wave in the corona. Although the eruptive active region is near the central meridian, several tens of degrees east of the footpoint of the nominal Parker spiral to the Earth, the kilometric spectrum of the type III bursts and the in situ detection of Langmuir waves demonstrate a direct magnetic connection between the L1 Lagrange point and the field lines onto which the electron beams are released at the Sun.

Conclusions. We interpret the forward- and reverse-drifting radio bursts as evidence of reconnection between the closed expanding magnetic structures of an erupting flux rope and ambient open magnetic field lines. We discuss the origin of relativistic particles near the Earth across two scenarios: (1) acceleration at the CME-driven shock as it intercepts interplanetary magnetic field lines rooted in the western solar hemisphere and (2) an alternative where the relativistic particles are initially confined in the erupting magnetic fields and get access to the open field lines to the Earth through these reconnection events.

Key words. acceleration of particles – Sun: coronal mass ejections (CMEs) – Sun: flares – Sun: particle emission – Sun: radio radiation – solar-terrestrial relations

1. Introduction

The Sun accelerates electrons, protons, and ions to suprathermal energies in a variety of transient events, ranging from small flares to coronal mass ejections (CMEs). The processes governing the acceleration and propagation are relevant for astrophysical plasmas in general. In the solar case, the available diagnostics of non-thermal particles are particularly rich, including their

electromagnetic emissions and measurements in space. In exceptional cases, particles are accelerated up to mildly relativistic energies, namely, GeV to tens of GeV for nucleons, and MeV for electrons. These particles are the focus of the present work.

Relativistic nucleons are detected through their gamma-ray emission in the solar atmosphere (e.g., Chupp & Ryan 2009; Share et al. 2018; Ajello et al. 2021, and references therein) and the cascades of secondary particles that they trigger in the atmosphere of the Earth (reviews in Lopate 2006; Belov et al. 2010).

⋆ Movie is available at https://www.aanda.org

On rare occasions, they can be measured in space by suitably equipped spacecraft (Bruno et al. 2018). Neutron monitors on the Earth are the standard equipment to measure the cascades triggered by particles with energies above a few hundreds of MeV, depending on the geographical location (Bütikofer 2018). These relativistic solar proton events are called ground-level enhancements or ground-level events (GLEs). The event on 2021 Oct. 28 is the 73rd event detected this way since 1942: GLEs are rare events, showing extreme particle energies in the context of solar activity.

GLEs are observed during eruptive solar events, with both enhanced electromagnetic emission and fast CMEs. During such events, charged particles are accelerated by small-scale processes related to magnetic reconnection and turbulence in a flaring active region (Cargill et al. 2012; Petrosian 2012) and at the coronal shock wave driven by the fast CME (Desai & Giacalone 2016). An introductory overview is given by Vainio & Afanasiev (2018). A fundamental difficulty of any attempt to relate particles detected near 1 AU to the parent solar processes is the propagation in the turbulent interplanetary magnetic field (e.g., Ch. 6 of Klein & Dalla 2017). A widely used criterion for connecting particles at 1 AU to the parent solar events is the timing, in particular, the solar release time of the first particles detected in space or on the Earth.

Radio and hard X-ray emissions are tracers of electron acceleration in the corona. In comparative studies the first relativistic protons were often found to arrive 10–20 min later than expected if their release occurred together with the acceleration of the first radiating electrons (Reames 2009; Aschwanden 2012; Gopalswamy et al. 2012). But during the strongest and best-observed GLE of the space age, on 2005 Jan. 20, no significant delay of the relativistic particle signatures was found (McCracken et al. 2008; Masson et al. 2009). This means that the timing of electron acceleration in the corona, taken as a proxy for charged-particle acceleration in general, and the release of relativistic protons to space involve processes of acceleration and propagation that may vary from event to event, and which are far from being fully understood.

The emission mechanism of hard X-rays is bremsstrahlung of non-thermal electrons as they impinge on the dense chromosphere in flaring active regions (e.g., Holman et al. 2011). Radio emissions in eruptive solar events are produced by various populations of non-thermal electrons (see reviews by Bastian et al. 1998; Nindos et al. 2008). Type III bursts are short (i.e., ∼1 s at m-λ, a few tens of seconds at decametre wavelengths) bursts that drift from high to low frequencies, ascribed to electron beams travelling outward through the corona along open magnetic field lines. The beams excite Langmuir waves that convert into radio waves and the emission therefore occurs at the electron plasma frequency or its harmonic. The sense of the drift hence shows the direction of the electron beams with respect to the gradient of the ambient electron density. Bursts with the opposite drift, but of similar duration and frequency-drift rate as the type III bursts, are called reverse-drift bursts and explained by sunward-propagating electron beams. Type II bursts are narrow bands of emission that drift more slowly than the type III bursts. They are ascribed to electrons accelerated at shock waves in the corona. Energetic electrons trapped in closed magnetic configurations are characterised by broadband continuum emission, known as a type IV burst. The emission may be incoherent gyrosynchrotron emission from mildly relativistic electrons or collective plasma emission. The emission frequencies depend on the magnetic field strength or the ambient electron density. Frequency drifts are explained by the confinement of electrons in expanding mag-

netic fields. The spectral features and locations of radio bursts can be exploited to study the acceleration and propagation of non-thermal electrons in the corona and the interplanetary space. Radio emissions offer various diagnostics for solar energetic particle research, as recently reviewed by Klein (2021a,b).

This study attempts to relate the early arrival time of relativistic particles near or at the Earth during the first GLE of solar cycle 25, on 2021 Oct. 28, with radio and X-ray signatures of electrons interacting in the solar atmosphere. The manuscript is organised as follows: Sect. 2 presents observations of the GLE and of electrons with similar speeds as the relativistic protons (Sect. 2.1), the related solar activity as observed in EUV and white-light images (Sect. 2.2), and signatures of electron acceleration in the corona at decimetric and longer wavelengths and in hard X-ray emission (Sect. 2.3). The magnetic connection of the Earth to the Sun is discussed in Sect. 2.4. The discussion (Sect. 3) starts with a summary of radio and hard X-ray observations. The observations are discussed in terms of two scenarios that are illustrated by a simple cartoon: the acceleration at the shock wave driven by the CME as it sweeps through the corona and the acceleration and trapping in erupting magnetic fields, followed by a gradual release due to reconnection with ambient open field lines.

2. Observations

2.1. Initial arrival of relativistic protons and electrons near Earth

The ground-level event (GLE) on 2021 Oct. 28 was observed by neutron monitors with nominal cutoff rigidities below about 2 GV, which corresponds to a kinetic energy of about 1 GeV. In the present analysis we consider standard neutron monitors with cutoff rigidities up to 1 GV. This corresponds to a kinetic energy of 450 MeV for a proton and is comparable to the minimum energy a proton needs to trigger an atmospheric cascade that is detectable at sea level. Mountain stations (South Pole, 2800 m asl) have a lower atmospheric energy cutoff near 300 MeV (Bütikofer 2018). The data were provided by the NMDB[1] data base with a time resolution of 1 min. The time histories of the neutron monitor count rates are plotted in Fig. 1. To reduce the noise, the median values of 1 min count rates of two high-altitude monitors (South Pole, red curve), of the two sea-level neutron monitors with the strongest response (Fort Smith FSMT, Peawanuk PWNK; black) and of the other sea-level neutron monitors (orange) are plotted. A more detailed analysis by Papaioannou et al. (2022) shows that at the onset of the GLE the SoPO, FSMT, and PWNK monitors have the asymptotic viewing directions closest to the interplanetary magnetic field. The plots show that the time profiles rise out of the background between 15:45 and 16:00 UT, with an earliest onset time estimate at 15:45 UT. To obtain a more objective estimate we fitted a straight line to the logarithm of the rise time profile, and evaluated the intersection with the pre-event background. Using an average of the neutron monitors with viewing directions close to the interplanetary magnetic field (SOPO, SOPB, FSMT, PWNK, Nain; central panel of Fig. 1) to increase the count rate statistics, we estimate the start at 15:46 UT ± 6 min. Papaioannou et al. (2022) report the earliest estimate of the GLE onset (South Pole, Calgary neutron monitors) at 15:45 UT, using data with 5 min integration.

The bottom panel of Fig. 1 shows the intensity-time profile of electrons in the nominal energy range (250–700) keV observed
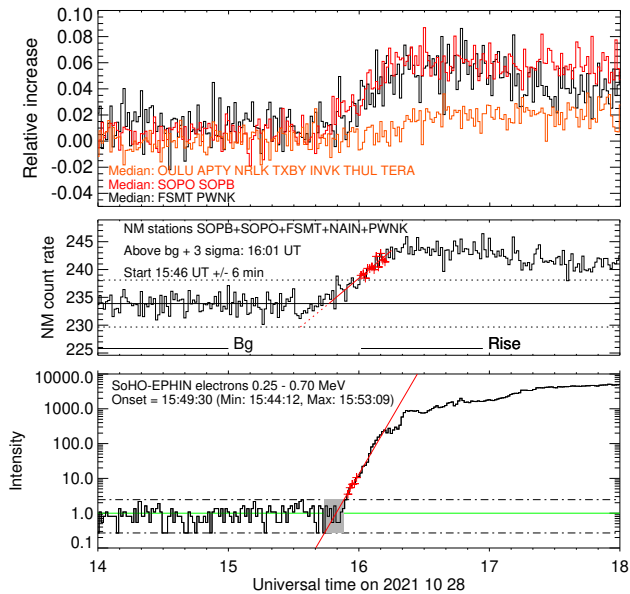
---

[1] www.nmdb.eu

Fig. 1. Time histories of the mean count rates of high-latitude neutron monitors (*top and central panel*) and of the intensity in the nominal (250–700) keV channel of SoHO/EPHIN (*bottom*). Horizontal lines in the central and bottom panels mark the constant background levels (solid) and the background $\pm 3\sigma$ levels (dashed). The red lines on the rising part of the profiles show linear fits to the logarithm of the count rate vs. time, the red plus-signs are the data points above background $+3\sigma$ used for the fits. The start times are the times when the straight line fits intersect the background. The quoted earliest and last possible onset times refer to the intersection of this fit with the background $\pm 3\sigma$.

by SoHO/EPHIN (Müller-Mellin et al. 1995). Data with a 1 min resolution were provided by the University of Kiel[2]. The speed of these electrons is comparable with the 1 GeV-protons. The onset time was also estimated by a linear fit to the logarithm of the intensity in the rise phase of the event. The latest possible onset is the time when the fit intersects the background $+3\sigma$. Relativistic electrons were found to start around 15:49:30 UT, with an uncertainty of about ± 5 min. An alternative approach using the Poisson CUSUM method (Huttunen-Heikinmaa et al. 2005) gives an onset time at 15:53–15:54 UT. The first relativistic electrons hence arrive at SoHO near the time of the GLE onset to within an uncertainty of several minutes that is mainly due to the weakness of the GLE.

With the solar wind speed of about 300 km s^{-1} measured near the Earth (see Sect. 2.4), a Parker spiral field line has a length of about 1.25 AU. Particles with a range of speeds $(0.75-0.87)c$, such as protons with kinetic energies in the range (0.45–0.94) GeV, need 3.5–5.5 min more to travel from the Sun to the Earth than electromagnetic waves. If we consider 15:40 UT as the earliest and 15:50 UT as the latest possible arrival time of the first relativistic particles, the solar release time is likely to be in the range (15:35–15:47) UT–500 s, with a considerable uncertainty due to the uncertain onset time of the protons and the unknown shape of the interplanetary magnetic field lines (see Sect. 2.4).

2.2. Parent solar activity

The GLE was associated with a solar flare of class X1.0 (SOL2021-10-28), reported by the NOAA Space Weather Prediction Center[3]. The soft X-ray emission in the 0.1–0.8 nm channel of the Geostationary Operational Environmental Satellite Program (GOES) started 15:17 UT and reached its maximum at 15:35 UT. The burst was reported to be accompanied by an optical flare of class 2N near central meridian, at S26° W05° as seen from the Earth. The corona was highly dynamic during the event, as shown, for instance, by the EUV movie at 17.1 nm wavelengths taken by the Atmospheric Imaging Assembly (AIA; Lemen et al. 2012) aboard the Solar Dynamics Observatory mission[4]. The parent active region shows changes since at least 15:05 UT, and expanding structures since about 15:20 UT. A wave-shaped feature expands initially mainly eastwards, starting from central meridian near 15:26 UT, and then into a broad range of directions from south-east over north to south-west since 15:32 UT. The exceptionally well-defined EUV wave reaches a small active region (NOAA 12890) in the south-western quadrant near 15:40 UT. The Proba 2/SWAP image[5] (Seaton et al. 2013) shows this active region near S20° W50°. The speed of the wave along a great circle on the solar surface inferred from the location and timing is about 690 km s^{-1}. The Large Angle and Spectrometric Coronagraph (LASCO, C2 Brueckner et al. 1995) aboard the Solar and Heliospheric Observatory (SoHO) saw a broad coronal mass ejection appear at the border of its occulting disk at 15:48 UT, which was fully developed from the east to the west limb (position angles 90° to 270°) in the subsequent images at and after 16:00 UT. The white-light image of the CME is highly structured with a corrugated front that advanced at a projected speed of about 1450 km s^{-1} between 15:48 and 17:00 UT. Papaioannou et al. (2022) evaluate speeds of 1240 and 1640 km s^{-1}, respectively, for the driver and the shock identified in the LASCO images. The EUV wave evolved from an erupting filament seen in the 17.1 nm images since 15:30 UT. The filament started near the central meridian and subsequently moved both outward and southward. This feature was probably the south-western leg of a loop-shaped structure that was observed above the LASCO/C2 occulter since 16:24 UT. The speed in the plane-of-the-sky of 360 km s^{-1} was inferred from LASCO images between 16:24 and 17:12 UT.

2.3. Electron acceleration in and escape from the corona

2.3.1. Instrumentation

In this section, radio and X-ray observations are used to infer the time history of non-thermal electrons in the corona. The radio data are dynamic spectrograms observed by the ground-based spectrographs EOVSA[6] (Extended Owens Valley Solar Array, 1–18 GHz, Gary et al. 2018), ORFEES[7] (144–1004 MHz, Hamini et al. 2021) at the Nançay Radio Observatory, by several e-CALLISTO spectrographs[8] (Benz et al. 2009), especially the one at Birr Castle, Ireland (Zucca et al. 2012) in

---

[2] http://www2.physik.uni-kiel.de/SOHO/phpeph/EPHIN.htm

[3] solarmonitor.org

[4] The movies were generated with the JHELIOVIEWER tool (Müller et al. 2017). The movie at 17.1 nm is available online

[5] https://www.solarmonitor.org/

[6] http://www.ovsa.njit.edu/

[7] https://rsdb.obs-nancay.fr/

[8] http://www.e-callisto.org/

the 22.25–87.69 MHz range, and by the WAVES spectrograph[9] (Bougeret et al. 1995) aboard the Wind spacecraft. Spikes and other signatures of terrestrial interference were removed from the data of the ground-based spectrographs. The observations from ORFEES were carried out after the antenna stopped tracking the Sun (15:09 UT, hour angle 52°). The observed flux densities were multiplied with a correction term evaluated from the analysis of the decay of the quiet-Sun emission during the same UT interval on October 27. The time resolution of the e-Callisto data is 0.25 s. The ORFEES data with 1 s or 0.1 s resolution were used. The Wind/WAVES data have a resolution of 16 s in the 14-1 MHz band and of 1 min at lower frequencies.

Hard X-ray imaging spectroscopy observations in the 4–150 keV range are provided by the Spectrometer/Telescope for Imaging X-rays (STIX, Krucker et al. 2020) on board Solar Orbiter (Müller et al. 2020). STIX is an indirect imaging system that reconstructs images from a set of 30 visibilities. For the analysis presented here, the calibration as of January 2022 has been used, which provides good calibration for 24 subcollimators with angular resolutions ranging from 14′ up to 180′ (for details we refer to Massa et al. 2022). The images shown in this paper are reconstructed using the CLEAN algorithm (Högbom 1974) adapted for STIX with a clean beam size of 16.5′ FWHM. At the time of the flare, Solar Orbiter was rather far away from the Sun at 0.80 AU, but the separation angle to the Earth-Sun line was only 4 deg. The small separation angle makes a comparison with observations taken from Earth relatively straightforward, but nevertheless, it is not possible to overlay images taken from Solar Orbiter with images obtained from Earth due to projection effects. As the STIX aspect system (Warmuth et al. 2020) is designed to only work at radial distances closer than 0.75 AU, we do not have image placement better than 10′ from STIX alone. Nevertheless, for large flares with clear non-thermal hard X-ray sources such as SOL2021-10-28, an accurate placement (i.e., better than a few arcsec) of STIX image can be obtained by comparing the STIX non-thermal sources with the brightest sources on the flare ribbons seen in UV and EUV, as observed by SDO/AIA.

2.3.2. Overview on radio and X-ray observations

Figure 2 shows the radio and X-ray time histories as tracers of energetic electrons interacting in the solar atmosphere. The hard X-ray (henceforth HXR) light curve at photon energies between 25 and 70 keV displays a rise to its peak at 15:28 UT, followed by a decay in several phases, including minor peaks. The microwave time profiles in the central panel are similar, but the late peaks are much more pronounced than in the HXR count rates. These late peaks show that electrons are injected into the low corona and chromosphere during the entire burst. The radio spectrum (top panel) is complex at cm-m-wavelengths (18 GHz–25 MHz), where bright bursts are superposed on a broadband continuum. The continuum starts at frequencies around 1 GHz, and then spreads gradually towards higher as well as lower frequencies. Three groups of type III bursts at frequencies below 20 MHz trace the escape of electron beams from the corona to the interplanetary space. They are henceforth referred to as DH type III bursts. The groups are labelled from 1 to 3 and delimited by dashed vertical lines in the spectrogram. The early phase of electron acceleration before group 1 has no radio signatures below about 100 MHz.
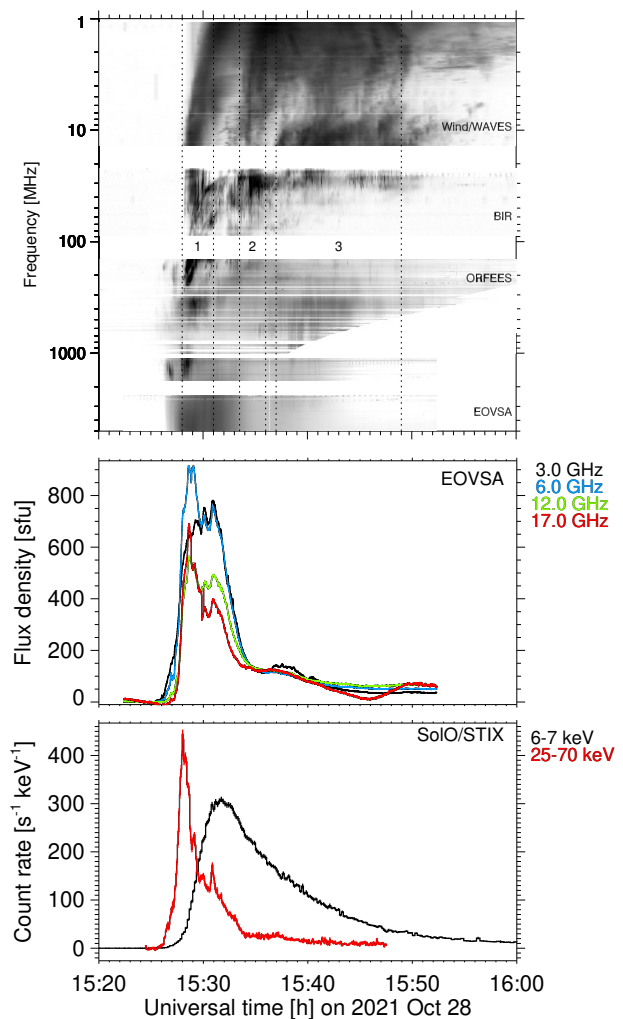
Fig. 2. Overview of the radio and X-ray emissions associated with the GLE on 2021 Oct. 28. *Top*: dynamic spectrogram in the range 1–5000 MHz observed by EOVSA, ORFEES, the e-Callisto station at Birr Castle (Ireland), and Wind/WAVES/RAD2. *Middle*: EOVSA light curves at four microwave frequencies. *Bottom*: solar Orbiter/STIX light curves in thermal (black) and non-thermal (red) X-rays. The vertical dashed lines delimit three numbered intervals of DH type III bursts.

The following subsections address successively the early acceleration (Sect. 2.3.3), the three groups of DH type III bursts and the accompanying metre-wave emission (Sects. 2.3.4–2.3.6), and the continuum (Sect. 2.3.7).

2.3.3. Early electron acceleration: 15:25–15:28 UT

This early episode of radio emission above 100 MHz accompanies the rise of the HXR burst until its peak (bottom panel of Fig. 3). The HXR time profile rises rather slowly between 15:25 and 15:27 UT, and then more steeply until the peak at 15:28 UT. Similar light curves are observed at microwaves (second panel from bottom) and in the 300–800 MHz range (second panel from top). They show the continuum from at least 18 GHz–300 MHz, with only a weak counterpart at 150 MHz during this early phase of radio emission.

At 1.5 GHz and lower frequencies this continuum underlies shorter bursts, which are more clearly seen in the time-difference spectrogram in the top panel of Fig. 3. The prominent bursts have a bandwidth of about 100 MHz. They occur initially
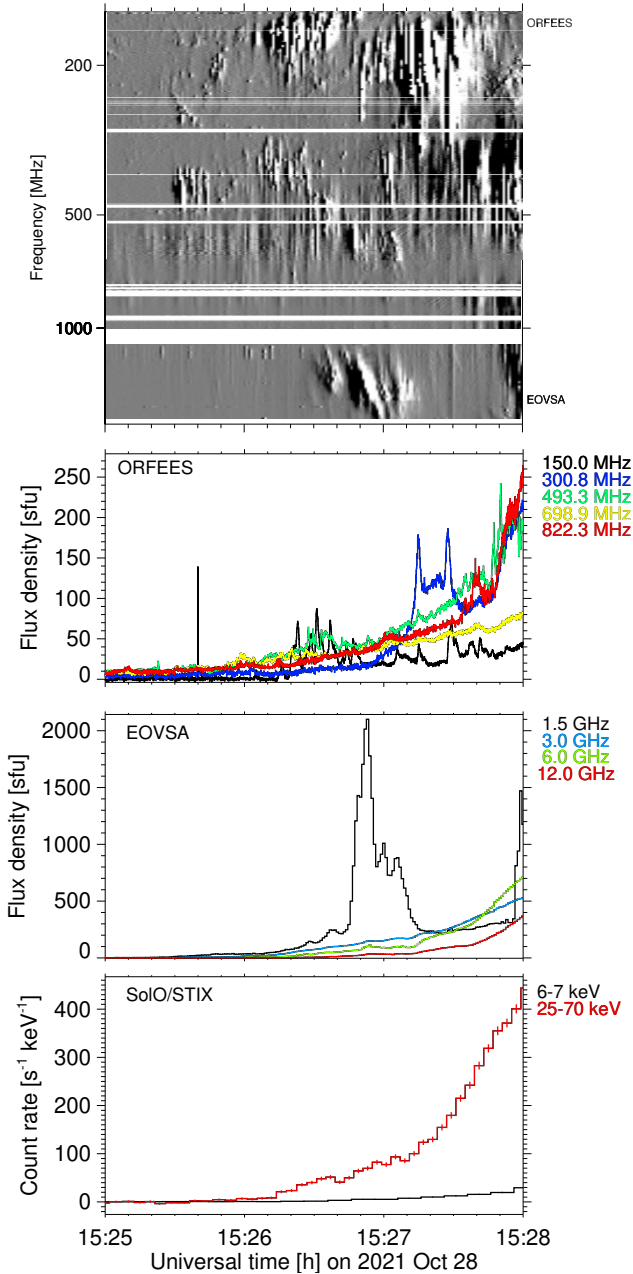
Fig. 3. Time-difference dynamic spectrogram (running difference spectra at 0.1 s time resolution for ORFEES and 1 s for EOVSA) in the range 144–1800 MHz, microwave (*middle panel*) and X-ray light curves (*bottom panel*) during the early phase of the radio event. The horizontal lines in the ORFEES spectrum and the vertical bars in the EOVSA spectrum between 1100 and 1200 MHz are terrestrial interference.

Table 1. Properties of fast-drift bursts in the 15:25–15:28 UT interval.

Time interval [UT]	Frequency range [MHz]	Spectrum
15:25:29–15:25:44	380–490	RS 0.19–0.27 s^{-1}
	<300	Spike bursts
15:26:00–15:26:30	321–393	RS 0.14 s^{-1}
	400–618	RS 0.06–0.10 s^{-1}
	<230	J-bursts
15:26:30–15:27:10	500–700	RS, overall drift → HF
	1100–1800	
15:26:59–15:27:01	347–469	RS, 0.18–0.20 s^{-1}
15:27:13–15:27:15	370–325	FWD (−0.07)–(−0.10) s^{-1}

In the two first intervals, the bursts in the high-frequency band drift from low to high frequencies. This shows electron beams moving downward from a coronal acceleration region (see review by Sinclair Reid & Ratcliffe 2014). In an isothermal hydrostatic model corona (cf. Appendix A) the logarithmic drift rates imply a radial speed on the order of 0.1c. The individual bursts scatter over different frequency ranges (e.g., the second group in Table 1) and often have spectral fine structure with irregular drifts. The bursts at frequencies below 300 MHz are initially spikes, then type J bursts, that is, bursts that drift to lower frequencies (forward drift) with a drift rate that decreases and eventually vanishes. They reveal electron beams that are released upward into the corona, but close to the top of a loop or a flux rope, where the beams propagate at a right angle to the density gradient, and the frequency drift vanishes. The start and end frequencies of the reverse-drift bursts vary, and the drift rates and frequency extent differ. Between 15:26:30 and 15:27:10, the start frequency of the reverse-drift bursts increases from about 300 to 500 MHz, and reverse-drift bursts also appear in the EOVSA spectrum. The third burst group (15:27–15:28 UT) is much more complex than the preceding ones. Forward- and reverse-drifting bursts are mixed in both the low-frequency and high-frequency groups, as illustrated by the two burst pairs 15:26:59–15:27:01 and 15:27:13–15:27:15 UT in Table 1 for the high-frequency band. They also cover the gap between the two frequency ranges observed before.

In the ORFEES spectrogram, less pronounced broadband pulsations are seen on top of the continuum in the spectral range down to the high-frequency burst group. The pulsations have no obvious frequency drift. A prominent example occurs shortly before 15:27 UT in the EOVSA spectrogram and down to 600 MHz in the ORFEES spectrogram. Broadband pulsations are a well-known fine structure of radio continua in the impulsive phase and in longer-lasting type IV bursts (Aschwanden 1987; Kliem et al. 2000; Aurass et al. 2003; Benz et al. 2011).

The strict low-frequency limit of the radio emission during this initial phase of the event suggests that the energetic electrons are radiating in closed magnetic structures. The high-frequency groups of mostly reverse-drift bursts show that electrons are released downward in magnetic structures in the low corona (typically extending up to, say, 0.1 $R_\odot$ above the photosphere, cf. the discussion of typical altitudes in Aschwanden 2002). The low-frequency limit of the continuum is near the range of these reverse-drift bursts. This is expected in the standard loop-shaped magnetic configuration of a flare, where non-thermal electrons are accelerated near the top and precipitated downward into the chromosphere. The configuration of the X-ray sources observed by Solar Orbiter/STIX in Fig. 4 confirms this picture: hard
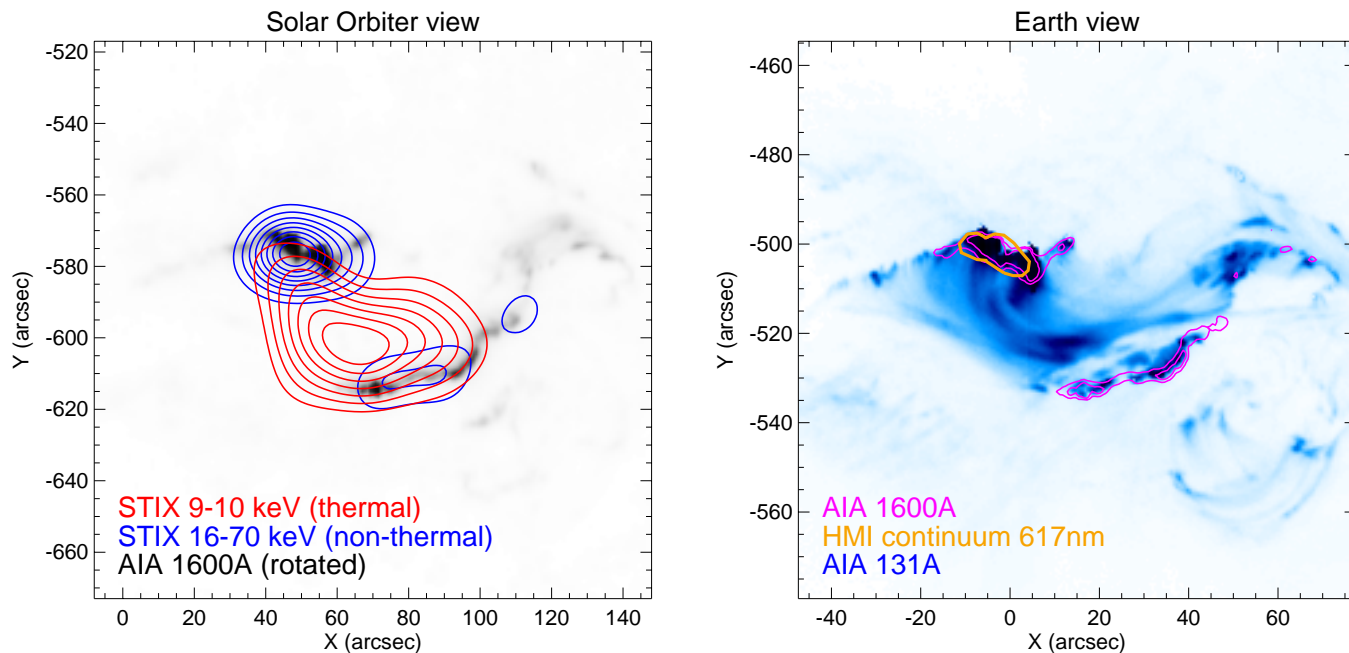
(15:25–15:27 UT) in two distinct frequency bands, respectively below and above 300 MHz, separated by a gap with a width comparable to the bandwidth of the bursts. The frequency of the gap varies with time. It disappears during the steep rise of the HXR profile. More detailed information on the bursts is listed in Table 1. The third column gives the type of the burst. "FWD" designates forward-drifting bursts, namely, bursts that drift from high to low frequencies in the course of time, "RS" means reverse-slope, that is, bursts drifting towards higher frequencies. The logarithmic drift rate is also given. It is derived here and in the following sections from a linear fit to the peaks of the burst in the ln(frequency)–time plane. The frequency range is estimated from a visual inspection of the dynamic spectrum.

Solar Orbiter view

Earth view

Fig. 4. Images of the flaring region in the chromosphere and low solar corona taken during the impulsive phase as seen from Solar Orbiter vantage point (*left*) and from Earth (*right*). On the left, STIX X-ray contours (15:27:24.6–15:28:09.6 UT) are plotted on top of a rotated AIA 1600A image (15:27:50.130 UT). The blue contours (20% through 90% at 10% spacing) correspond to the non-thermal emissions from the flare ribbon outlining the main source of precipitation of flare-accelerated electrons. The non-thermal sources are well correlated with the locations of the main UV 1600A sources. Thermal X-ray emissions (contours from 30% to 90%) are seen from loops connecting the hard X-ray sources. From Earth view (*right*), the AIA 131A image from 15:28:06.620 UT shows both the flare ribbons as well as the loops connecting the ribbons. For reference with the Solar Orbiter view, the AIA1600A are shown as magenta contours (20% and 50% levels). HMI continuum observations reveal a white light flare source (orange contours at 80% of the peak value at 15:28:12 UT), but only the northern ribbon is seen while the signal-to-noise ratio of the southern ribbon appears to be too low to be visible above the non-flare related solar variations detected by HMI.

X-rays come from a double source (blue contours), and soft X-rays (red contours) from a single source projecting in between. A visual comparison with the SDO/AIA movie suggests that the X-ray sources lie below the erupting filament, which rises in the south-eastward direction above the parent active region.

2.3.4. Non-thermal electron escape: the first group of DH type III bursts, 15:28–15:31 UT

The radio spectrum changes at the time of the HXR peak, which denotes the start of the electron release to the interplanetary space with the first DH type III group (interval 1 in Fig. 2). In the dynamic spectrogram in Fig. 5 the type III bursts start in the frequency range between 50 MHz and two parallel-drifting bands of emission in the ORFEES spectrum, which are part of a type II burst produced by a coronal shock wave. The bands have a frequency ratio of 1.33 and a logarithmic drift rate of $-9.27 \times 10^{-3}\,\mathrm{s}^{-1}$. At frequencies below 85 MHz the e-Callisto spectrogram shows narrow curved bands. One is near 40 MHz at 15:30 UT, when the upper limit of the type II emission that extends the high-frequency band observed by ORFEES is near 80 MHz. This means that the curved bands belong to fundamental emission of the type II burst, although their shape contrasts with the straight-line shape of the harmonic. The type II bands can be tracked down to 23 MHz in the e-Callisto observations. The type II bands seen by ORFEES are hence split bands of harmonic emission. Two red dashed lines are overlaid on the spectrogram to guide the eye. They display the harmonic lane through the low-frequency split band and its fundamental, as inferred from the model described in Appendix A.

2.3.5. Non-thermal electron escape: the second group of DH type III bursts, 15:33:30–15:36 UT

In the Wind/WAVES spectrum, the second DH type III group is observed starting about 15:33:30 UT. In the light curve at 10 MHz, displayed in the top panel of Fig. 6, the strongest type III emission is seen between 15:34 UT and 15:34:40 UT. The type III bursts are preceded by some patchy emission between 14 and 5 MHz since 15:32 UT (Fig. 2), which may be an early type III burst or an early manifestation of a hectometric type II burst.

Figure 6 displays the HXR and metre-wave radio emission starting 1.5 min before the DH type III bursts, which begin at the vertical dashed line. The HXR count rate (in red, bottom panel) decreases, with weak superposed variations, until 15:34 UT. At this time the signal is still above the pre-event background, as seen in Fig. 2. The microwave emission (not shown) behaves the same way. The dynamic metre-wave spectrum in the central panel of Fig. 6 shows the continuum, which reaches the low-frequency border of the ORFEES receiver near 15:34 UT. On its low-frequency side, the ORFEES and e-Callisto spectrographs see burst groups with complex spectral structure. The characteristic features of different groups are listed in Table 2:

- The brightest bursts in the ORFEES spectrogram are reverse-drift bursts (15:32:21–15:34:05 UT), extending from its low-frequency border (144 MHz) up to about 220 MHz, in the strongest burst to 256 MHz. They start near 50 MHz in the e-Callisto spectrograms.
- This group is preceded in the ORFEES spectrogram (15:32:10–15:32:21 UT) by a group of forward-drifting
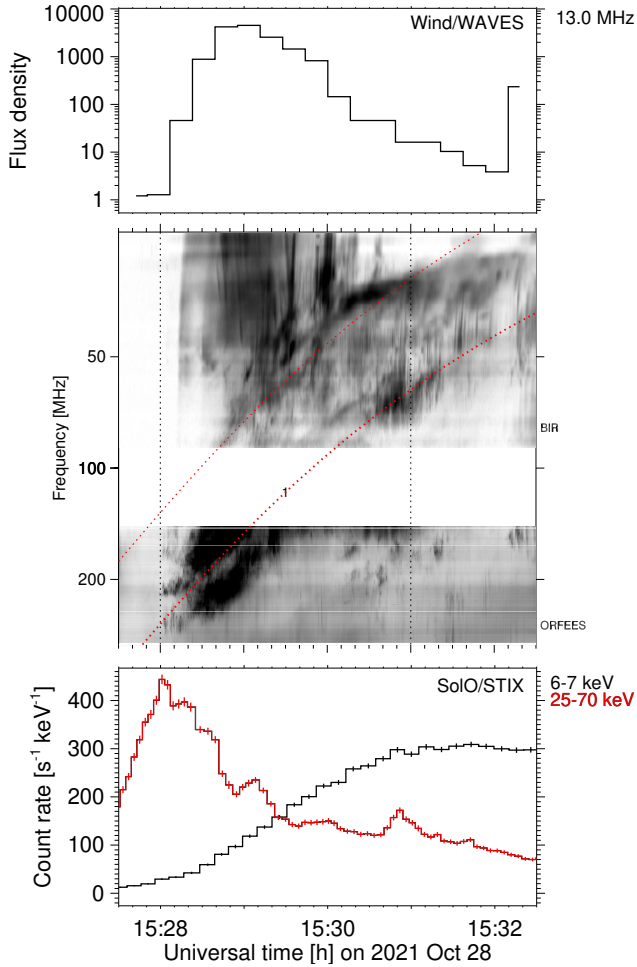
Fig. 5. Light curves of radio emission at decametre-λ (*top*), dynamic spectrogram at m-λ (*centre*), and X-ray light curves (*bottom*) during the first DH type III group on 2021 Oct. 28, which is delimited by the vertical dashed lines (see Fig. 2). The red dotted lines show the trajectories of the fundamental and harmonic lanes of a model type II (see Sect. A).
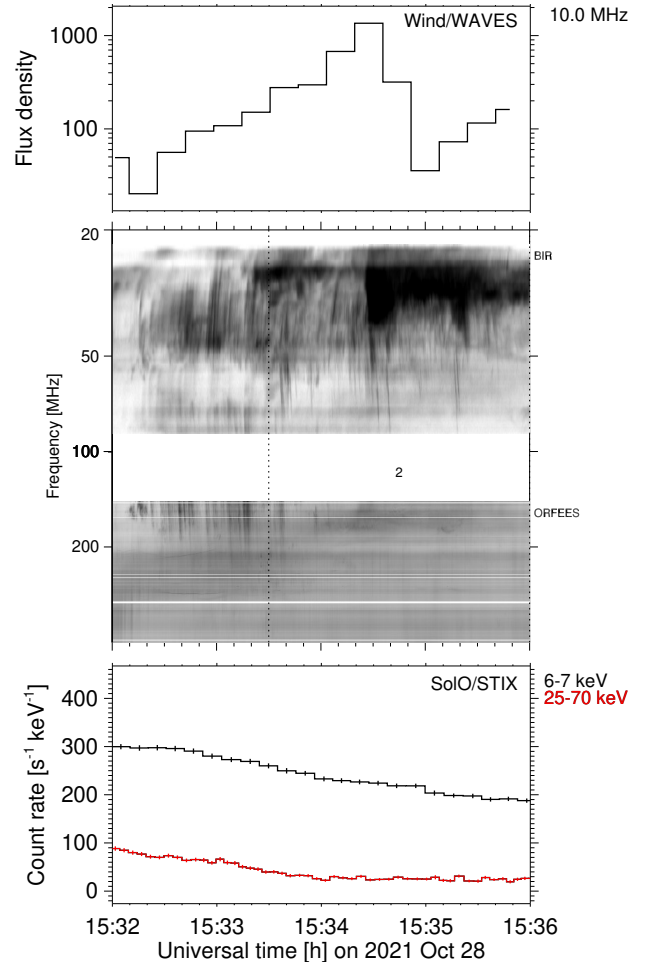

Fig. 6. Light curves of radio emission at decametre-λ (*top*), dynamic spectrogram at m-λ (*centre*), and X-ray light curves (*bottom*) during the second DH type III group on 2021 Oct. 28, which starts at the vertical dashed line (see Fig. 2).

Table 2. Properties of fast-drift bursts at metre-wavelengths prior to and during the second group of DH type III bursts.

Time interval [UT]	Frequency range [MHz]	Spectrum
15:32:10–15:32:21	169–50	J
15:32:22–15:34:02	50–256	RS 0.19–0.41 s^{-1}
15:32:15–15:34:10	50–($\leq$)25	III (−0.12)–(−0.18) s^{-1}
15:33:35–15:33:40	49–78	RS 0.19–0.20 s^{-1}
	46–34	III (−0.13)–(−0.23) s^{-1}
15:34:28–15:35:19	52–(>)85	RS 0.15–0.27 s^{-1}
15:35:28–15:35:41	34–57	RS 0.19–0.22 s^{-1}

bursts. Their drift is not obvious in this figure, but becomes clear in the time-difference spectrum (not shown). The bursts are observed in the e-Callisto spectrogram down to about 50 MHz, which is the start frequency of the subsequent reverse-drift bursts. The frequency drift vanishes there. These bursts are type J bursts.

- During the type J and reverse-drift bursts above 50 MHz, the e-Callisto spectrograms show type III bursts extending from the same frequency 50 MHz to the low-frequency border of the receiver at 22 MHz. These are the high-frequency counterparts of the patchy emission between 14 and 5 MHz, which may be early manifestations of DH type III bursts.
- A short group of forward/reverse drift bursts (15:33:35–15:33:40 UT) shows, once again, the separation at 50 MHz.

The strongest DH type III burst, taking place shortly after 15:34 UT, is accompanied at metre wavelengths by reverse-drifting bursts. The most prominent examples listed in Table 2 have a higher flux density and broader spectral extent in the e-Callisto spectrum than before 15:34 UT. The separation of burst types at 50 MHz, which was prominent in the previous bursts, has disappeared. The start frequency now scatters between 34 and 52 MHz. The spectral shape at frequencies below 30 MHz at the start of the intense emission at 15:34:25 suggests that forward-drifting bursts are observed there, which may be the

high-frequency part of the DH type III bursts. Their rate of occurrence is so high that individual elements can no longer be identified.

2.3.6. Non-thermal electron escape: the third group of DH type III bursts, 15:38–15:49 UT

The third group of type III bursts is longer than the others. The dynamic spectrogram in the central panel of Fig. 7 shows that the type III bursts emerge out of an intense emission extending
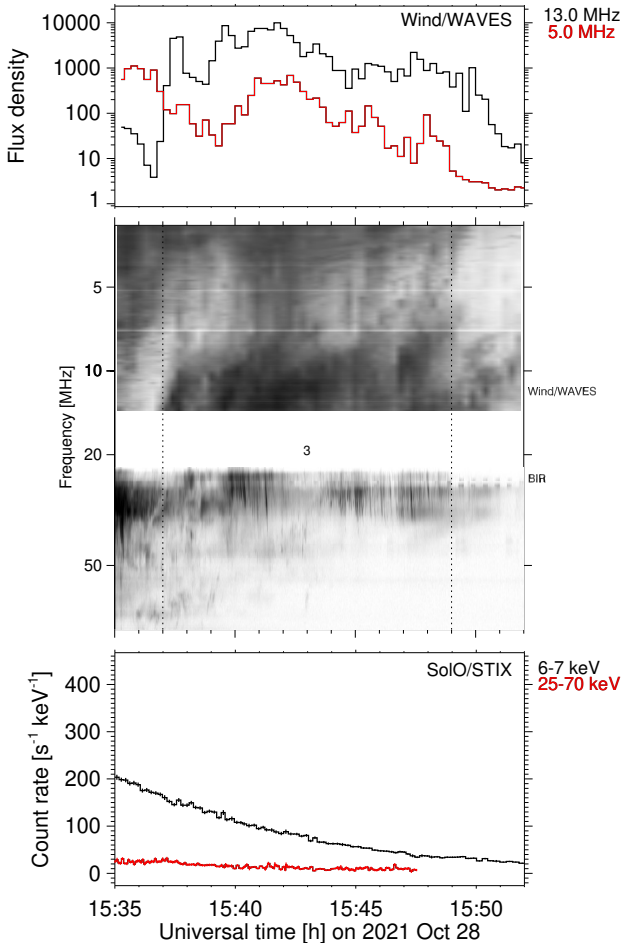
Fig. 7. Light curves of radio emission at decametre-λ (*top*), dynamic spectrogram at m-to-decametre-λ (*centre*), and X-ray light curves (*bottom*) during the third DH type III group, delimited by the pair of vertical dashed lines (see Fig. 2).

down to about 8 MHz. The WAVES spectrum shows traces of fast-drift bursts, but the 16 s time resolution is not enough to clearly identify individual bursts. This is confirmed by the two single-frequency records in the top panel. The metre-wave counterparts are now at lower frequencies than before. The dominant features in the e-Callisto spectrographs are reverse-drift bursts, which start in the unobserved range between 14 and 22 MHz and extend to about 40 MHz.

The reverse-drift bursts in the e-Callisto spectrograms occur in two groups, with weaker, but still significant, activity between 15:42 and 15:44 UT. The characteristics are listed in Table 3. It is mostly the flux density and the occurrence rate of the bursts that are reduced in the 15:42–15:44 UT interval. On a few occasions forward-drifting bursts are seen between the reverse-drifting ones.

2.3.7. Confined non-thermal electrons in the corona

Thus far, we have discussed the radio and X-ray emission during the early electron release into confined magnetic structures and the radio emission near the start frequency of the three groups of DH type III bursts. At higher frequencies (i.e., frequencies above the metre-wave type II burst and above the groups of forward-and-reverse-drifting bursts accompanying the DH type III bursts), the continuum emission continues throughout and after the decay of the HXR count rate. The continuum gradually proceeds to lower
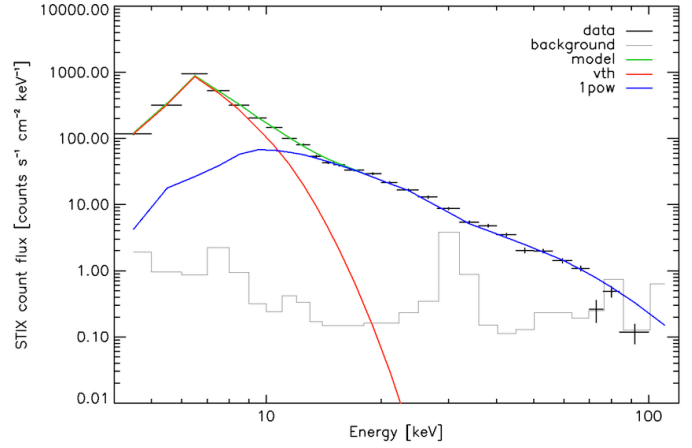

Fig. 8. X-ray count flux spectrum from STIX observations, at 15:27:59 UT with an integration over 0.5 s. The observed count flux is shown by the thick black crosses, the pre-flare background spectrum is shown by the thin black line, and the fitted spectrum is shown by the green line. The thermal component of the fitted model is shown in red, and the non-thermal power-law component is shown in blue.

Table 3. Properties of fast-drift bursts at metre-wavelengths during the third group of DH type III bursts.

Time interval [UT]	Frequency range [MHz]	Spectrum
15:39:30–15:42:00	(<)23–41	RS $(5.7\text{–}7.4) \times 10^{-2}$ s^{-1}
15:42:00–15:44:00	23–34	RS $(6.2\text{–}8.6) \times 10^{-2}$ s^{-1}
15:44:00–15:49:45	(<)23–39	RS $(7.1\text{–}12) \times 10^{-2}$ s^{-1}

frequencies, while minor peaks in the early decay phase of the HXR light curve and the conspicuous second peak at microwave frequencies indicate new episodes of electron acceleration. The radio continuum is observed down to the ORFEES low-frequency limit at 144 MHz after about 15:34 UT. Because of its long duration, this continuum is a type IV burst and the smooth spectrum suggests a pursuit of the gyro-synchrotron emission of relativistic electrons observed earlier. Near its low-frequency edge the overview spectrum (Fig. 2) shows some weak patches of emission with smaller bandwidths, which systematically drift towards lower frequencies. They are surrounded by the blue parallelogram in the annotated dynamic spectrum (shown in Fig. 12). Closer examination shows that these features are continuum enhancements with embedded bursts of 10–20 MHz bandwidth. Some of them show reverse drifts, whereas in others, no drift is recognisable. Similar emissions are visible on the high-frequency side of the metric type II burst in Fig. 5 (15:30–15:31:30 UT, below 220 MHz) and possibly down to 50–60 MHz in the e-Callisto spectrogram.

The rather well-defined low-frequency limitation of the type IV continuum with the drifting patches again reveals confined electrons, with no signature of direct escape. The drift towards lower frequencies can be explained by an outward expansion of the confining magnetic field structures. This could be a moving type IV burst, but we have no imaging observations to confirm this identification. The radio emission is accompanied by faint HXR emission, which justifies a lean towards Carley et al. (2016) and calling it a flare continuum (cf. Pick 1986).

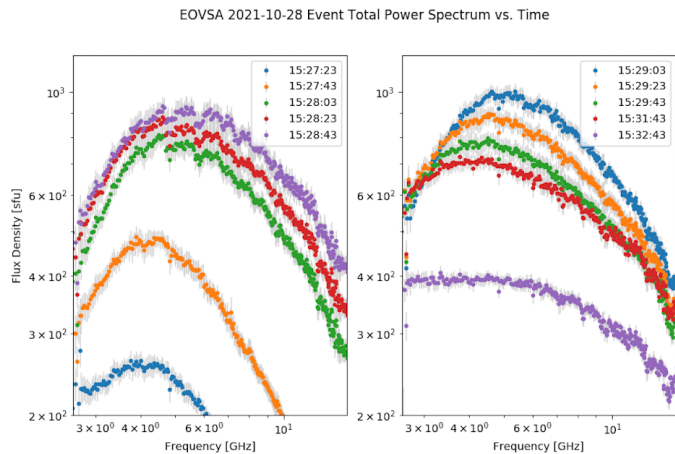Further evidence on confined non-thermal electrons is provided by the HXR and microwave spectra. The X-ray

Fig. 9. Total-power spectrum of the microwave emission at selected times during the rise (*left panel*) and decay phase (*right panel*) of the microwave burst observed by EOVSA.
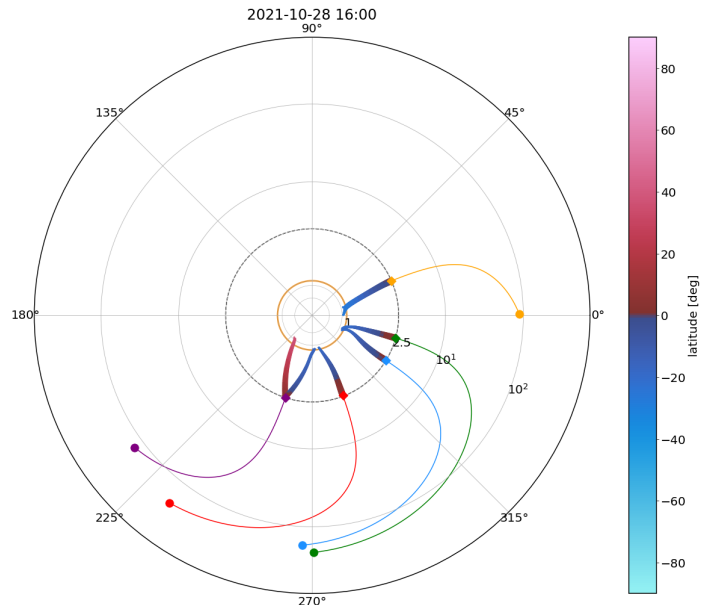

Fig. 10. Magnetic connection to the Sun by interplanetary Parker-spiral field lines and PFSS modelling on 2021 Oct. 28 16:00 UT. The vantage points are (*from left to right*) Parker Solar Probe, STEREO A, Solar Orbiter (blue), the Earth (green), and Bepi Colombo. The field lines are Parker spirals for the measured solar wind speed between the vantage point ($305 \, \mathrm{km \, s^{-1}}$ for the Earth/L1) and the solar wind source surface at heliocentric distance $2.5 \, R_\odot$ (logarithmic distance scale) and a potential field-source surface extrapolation of the photospheric magnetogram from the source surface to the solar photosphere (linear distance scale. The colour code of the PFSS field lines shows the heliocentric latitude, from southern latitudes in blue to northern latitudes displayed in red shading.

spectrum around the peak of the non-thermal X-ray emission, at 15:27:59 UT, is shown in Fig. 8. This spectrum was fitted with a thermal component and a single power law, with a plasma temperature of $15.9 \pm 0.3 \, \mathrm{MK}$, an emission measure of $(1.7 \pm 0.2) \times 10^{48} \, \mathrm{cm^{-3}}$, and a negative spectral index γ of the photon spectrum of 2.5 ± 0.1. This value of the spectral index is on the lower end of the statistical distributions of γ for flares observed by previous missions such as ICE/ISEE-3, SMM/HXRBS and RHESSI (Hannah et al. 2011), which means that the photon spectrum is particularly hard; in fact, it continues to harden throughout the rise phase. The hardening can be tracked until 20 s after the peak. It is clear that the spectral evolution suggests a continued hardening throughout the peak, rather than the soft-hard-soft evolution that is typical of impulsive hard X-ray bursts (see Sect. 1.3 of Fletcher et al. 2011, and references therein).

Microwave spectra observed by EOVSA are displayed in 20-s time steps in Fig. 9 during the rise phase (left panel) and the decay phase (right panel) of the event. During the rise phase, the spectral peak shifts from lower to higher frequencies, which is in line with the expected evolution of a gyro-synchrotron spectrum when the number of non-thermal electrons increases. At frequencies above 10 GHz, the trend of the decay of the spectrum clearly indicates that the higher the frequency, the slower the decay. In a single source of gyro-synchrotron emission, this behaviour points to the gradual hardening of the electron spectrum, as does the hardening of the HXR spectrum.

In summary, both the morphology of the radio spectrum at decimetre-to-metre wavelengths and the hardening of the HXR and microwave spectra are consistent with non-thermal electrons that are confined in evolving magnetic fields in the corona.

2.4. Magnetic connection between the Earth and the solar activity

The parent active region of the 2021 Oct. 28 GLE is at central meridian in the southern solar hemisphere. This region is not connected to the Earth by a Parker spiral interplanetary magnetic field line. Figure 10 shows the connections by nominal Parker spirals of different points in the solar system with the solar wind source surface at a supposed heliocentric distance of $2.5 \, R_\odot$. The Parker spirals are determined by the solar wind speed measured at the various spacecraft (i.e., $305 \, \mathrm{km \, s^{-1}}$ at the Earth/L1). The radial distance scale is logarithmic at heliocen-

tric distances beyond the source surface, and linear within the source surface. The fat curves between the source surface and the solar photosphere are bundles of field lines computed by a potential field-source surface (PFSS) extrapolation of an HMI synoptic map provided by the Joint Science Operations Center (JSOC)[10]. The Earth is found to be connected to N5° W74° on the source surface, and S21° W65° on the photosphere. The prediction is hence a good connection to the parent active region in latitude, but a distance of more than 60° in heliolongitude. The model shows the spreading of open field lines between the active region and the source surface, such that the same photospheric connection is found for Solar Orbiter.

From these considerations, it would be expected that the Wind spacecraft does not intercept the electron beams emitting the different groups of type III bursts. This is, however, contradicted by the observations. The dynamic spectrogram at kilometric wavelengths, as observed by Wind, is plotted in the top panel of Fig. 11. The bottom panel displays the difference between adjacent frequencies. The differencing reduces artefacts in the original spectrum, where strong emission at high frequencies spills over into the low-frequency receiver channels creating rectangular structures in the dynamic spectrogram, with a sharp cutoff at the borders of individual receivers. The enhanced narrow band of emission before the type III burst, which has a continuous slow drift from 30 kHz (14:00 UT) to slightly higher frequencies at 16:20 UT, is the local plasma line, namely, thermal plasma emission generated by Langmuir waves in the vicinity

---

[10] We use the hmi.Synoptic_Mr_720s maps provided at http://jsoc.stanford.edu/HMI/LOS_Synoptic_charts.html
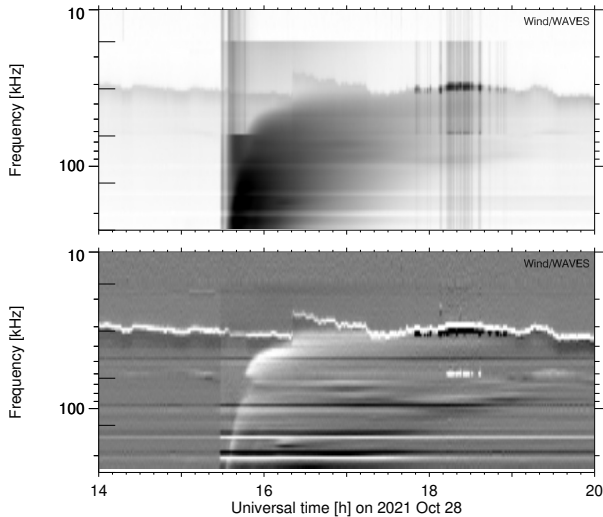
Fig. 11. Dynamic spectrogram at km-wavelengths observed by Wind/WAVES/TNR (*top panel*) and frequency-difference spectrum of TNR (*bottom*). Vertical bars in the top panel are artefacts, due to the spillover of intense emission in some channels to the entire receiver.

of the spacecraft. The drift to higher frequencies shows a slow increase of the ambient electron density at the spacecraft.

There are two indications showing that the spacecraft is on the field lines guiding the electron beams from the Sun. The clearest one is the detection of packets of Langmuir waves between 17:50 and 18:55 UT. It is known that Langmuir waves cannot propagate out of their source and, thus, their detection demonstrates that the spacecraft is intercepting the parent electron beams. The fact that the low-frequency edge of the type III spectrum joins the plasma line near 16:20 UT is another proof that the spacecraft intercepts the electron beams. There is some complexity involved, because the plasma line jumps to lower frequencies near 16:20 UT. This jump is accompanied by a sudden change of the magnetic field orientation and a subsequent rotation of the magnetic field seen in measurements aboard the Wind spacecraft (not shown here). This indicates that a different magnetic structure, probably a flux rope, crosses the spacecraft. Judging from the frequency-difference spectrum in Fig. 11, the low-frequency edge of the type III spectrum does not extend to the plasma line in this flux rope, but stays at the frequency where it was before the jump. This means that the type III-burst-emitting electrons are in the structure to which the spacecraft is connected before 16:20 UT and after about 17:15 UT. For the latter discussion of the nature of the magnetic connection, we add that the dynamic spectrum observed by the WAVES spectrograph aboard STEREO A (Bougeret et al. 2008, not shown here) exhibits Langmuir waves between 16:50 and 17:30 UT, which overlaps with the time interval of Langmuir waves at Wind, and between 18:25 and 18:50 UT. Langmuir waves were also detected at Solar Orbiter and Parker Solar Probe (Maksimovic, priv. comm.).

If the time when the leading edge of the type III spectrum joins the plasma line at Wind, 16:20 UT, is the arrival time of the electrons that emit the radio emission, the start of the metric type III burst around 15:28 UT–500 s implies an interplanetary travel time of 1 h. With a field line length 1.3 AU this gives an average speed of $0.18c$ and a kinetic energy of 9 keV. These values are within the commonly quoted range of average exciter speeds of type III bursts near 1 AU (Hoang et al. 1994; Buttighoffer 1998; Ergun et al. 1998; Reiner & MacDowall 2015).

Table 4. Time lines of the radio, hard X-ray (HXR), and initial relativistic particle emission on 2021 Oct. 28.

UT interval	Spectral range	Observed feature
15:25–15:28	HXR	Rise of count rates to their peak
(Fig. 3;	18 000–300 MHz	Continuum, broadb. pulsations
Sect. 2.3.3)	650–300 MHz	Reverse-drift bursts
	300–144 MHz	Type *J* bursts
	≤85 MHz	No signal
15:28–15:32	HXR	Peak and early decay;
(Fig. 5;		hardening spectrum
Sect. 2.3.4)	18 000–300 MHz	Type IV burst
	300–25 MHz	Type II burst
	≤50 MHz	First group of type III bursts
15:32–15:36	HXR	Decay
(Fig. 6;	SXR	Peak at 15:35 UT
Sect. 2.3.5)	18 000–(<)144 MHz	Type IV burst
	200–25 MHz	Forward-/reverse-drift bursts
	≤14 MHz	Second group of type III bursts
15:37–15:50	HXR	No signal after 15:40 UT
(Fig. 7;	1000 (?)–25 (?) MHz	Type IV burst
Sect. 2.3.6)	50–25 MHz	Forward-/reverse-drift bursts
	14–7 MHz	Continuum, unresolved bursts?
	≤7 MHz	Third group of type III bursts
15:35–15:46	Particles	Initial release window
(Fig. 1;		(uncertainty) of
Sect. 2.1)		electrons, protons >0.75c

The open field lines near the parent active region shown by the PFSS extrapolation have negative polarity, namely, they are sunward-directed, as are the field lines at Wind. Another group of open field lines, with the same magnetic polarity, is rooted near active region NOAA 12890 in the western solar hemisphere.

3. Discussion

3.1. Summary of solar observations

The hard X-ray and radio emission in the solar atmosphere reveals several sources of interacting and escaping non-thermal electrons during the 2021 Oct. 28 event. Different episodes are summarised in Table 4, and features of the radio spectrum that are essential for the discussion are annotated in the dynamic spectrogram in Fig. 12.

– During the first three minutes electrons radiating hard X-rays are closely related with electrons emitting radio waves at centimetre-to-decimetre wavelengths (frequencies ≥300 MHz). The radio emission consists of short, band-limited bursts on top of a smoothly evolving continuum that gradually extends from about 1 GHz to both higher and lower frequencies. The smooth frequency spectrum suggests that the continuum is produced by gyrosynchrotron emission of relativistic electrons (see reviews in Bastian et al. 1998; Nindos et al. 2008).

– The gradual extension of the 1–18 GHz onset towards higher frequencies shows the gradual increase of the number of non-thermal electrons. This is in line with the typical increase of the peak frequency during the rise of microwave bursts (Melnikov et al. 2008).

– The well-defined low-frequency limit of the continuum and the bursts during this phase, the ubiquity of reverse-drift bursts, and the hard X-ray source geometry suggest that the
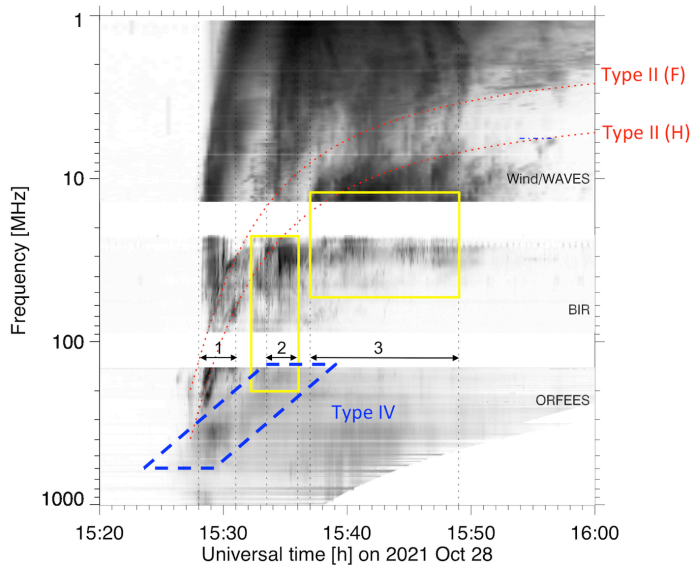
Fig. 12. Dynamic spectrogram from 1004 to 1 MHz, with the suggested spectral identifications annotated. See text for more details.

electrons are emitting in closed magnetic structures in the low corona with an acceleration region near its top.

- The hard X-ray and microwave spectra harden throughout the rise and at least the early decay phase. This behaviour is different from common impulsive hard X-ray bursts, where the photon spectrum hardens until the peak, but softens thereafter (see review by Fletcher et al. 2011, and references therein). The persistent hardening is consistent, for instance, with a non-thermal electron population trapped in magnetic fields.
- The low-frequency border of the continuum and the bursts drift towards lower frequencies throughout the event, starting in the early phase. This implies the expansion of the closed magnetic structures, as expected during a CME. A specific drifting signature is delimited by the blue dashed parallelogram in Fig. 12. This emission is a type IV burst.
- The escape of energetic electrons to the high corona and the interplanetary space is traced by three successive groups of type III bursts, which are especially clear at decametre and longer wavelengths (frequency ≤14 MHz). The burst groups are labelled 1–3 and delimited by vertical dashed lines in Fig. 12.
- The first group of type III bursts starts at metre-wavelengths, at the time of a type II burst and on its low-frequency side.
- At the times of the second and third group of type III bursts, which start at decametre wavelengths (frequency <30 MHz), groups of forward-reverse drift bursts are observed in the metre-wave spectrum (two yellow rectangles in Fig. 12). The type III bursts occur during the decay (second group) and persist after the end of the HXR and microwave emission (third group).
- The low-frequency edge of the type III spectrum at km-wavelengths (≃30 kHz) and the detection of Langmuir waves at Wind show that the radio-emitting electrons reach the spacecraft, which is hence magnetically connected to the open field lines in the corona onto which the electron beams are released. The magnetic field lines at the spacecraft have the same polarity as the open field lines in the parent active region of the eruptive event, NOAA 12887, and in two

small active regions (NOAA 12890 and 12885) in the south-western solar quadrant.

- The initial release of relativistic protons and electrons towards Earth is estimated to occur during the third group of DH type III bursts.

3.2. The type II burst

Type II emission from a coronal shock wave is most obvious at metre-wavelengths during this event. This shock wave occurs early, starting at the time of the hard X-ray peak. No direct extension is seen into the decametric-to-hectometric range. This can be due to the bright type III bursts, which cover the entire frequency range of Wind/WAVES between the start of the metre-wave type II burst and 20 min later. After their end, different narrow drifting bands, lasting a few minutes each, are scattered over the range 1–4 MHz, and a long-lasting emission is seen at frequencies below 3 MHz (Fig. 12). The latter can be identified as a background behind the DH type III bursts. The high-frequency border drifts gradually to lower frequencies. This and the scattered drifting bands are likely another manifestation of type II emission, which may or may not be the continuation of the early metre-wave type II burst.

A model spectrum of a type II burst that connects the early metre-wave and later decametre-hectometre-wave signatures is discussed in Appendix A. The fundamental and harmonic track inferred from the model are overplotted as dashed red curves on the dynamic spectrum in Fig. 12, labelled "Type II (F)" and "Type II (H)", respectively. But the type II manifestations in the two spectral ranges may also be independent, for instance, if the early metre-wave type II burst results from a blast wave that vanishes near the end of the metre-wave signature around 15:32 UT, while the DH signatures are due to the CME-driven shock. The near simultaneity of the hard X-ray peak, which signals the time of strongest impulsive energy release and the start of the type II burst near 300 MHz supports this interpretation. The question of whether type II bursts reveal blast waves or driven shock waves is widely discussed in the literature (see reviews by Vršnak & Cliver 2008; Carley et al. 2020). The distinction is not essential for the present discussion of particle acceleration scenarios.

The metre-wave type II burst has well-defined split bands. The ratio of plasma densities in the sources is the square of the measured frequency ratio 1.33, that is, $X = 1.78$. Split bands are often ascribed to simultaneous emission upstream and downstream of the shock wave (Smerd et al. 1975; Vršnak et al. 2001), but the interpretation is subject to debate (e.g., Cairns 2011, and review in Ch. 2.2 of Klein 2021b). Within this hypothesis, and based on the assumption that the type II source is at a quasi-perpendicular shock front (e.g., Mann et al. 2018), the compression ratio implies an alfvenic Mach number of around 2, depending on the polytropic index and the plasma β, and a fast magnetosonic Mach number of 1.6. Hence, this shock, as in the case of most shocks probed through the band-splitting diagnostics, is rather weak. This may be a general property of shock waves that generate type II bursts. Mann et al. (2022) show that the competition between the convective electric field accelerating electrons at a quasi-perpendicular shock and the oppositely acting cross-shock potential, which both increase with increasing Alfvenic Mach number M_A, creates optimal conditions for the generation of Langmuir waves at moderate Mach numbers, near $M_A = 1.9$ (their Table 1).

In an isothermal hydrostatic coronal model the logarithmic drift rate is related to the radial component of the exciter speed by Eq. (A.2). For a given coronal temperature, for instance,

1.4 MK in the Newkirk model (Newkirk 1967), the only free parameter is the heliocentric distance of the radio source. The heliocentric distance of the harmonic type II source at 180 MHz was inferred to be $1.2\,R_\odot$ from the combined model of the metric and the DH type II burst in Appendix A. This is a plausible value, given, for instance, the locations of type III burst sources (Saint-Hilaire et al. 2013). The radial component of the exciter speed in the metre-wave source is then $1900\,\mathrm{km\,s^{-1}}$, with an overall speed of $2600\,\mathrm{km\,s^{-1}}$. This estimate remains valid even if the metre-wave type II burst has no DH-continuation. The fast magnetosonic speed inferred at $1.2\,R_\odot$ from a Mach number of 1.6 and a shock with speed $1900{-}2600\,\mathrm{km\,s^{-1}}$ is in the range $1200{-}1600\,\mathrm{km\,s^{-1}}$, which is consistent with the maps derived by Warmuth & Mann (2005) and Zucca et al. (2014). The start of the first group of DH type III bursts at the time of the metre-wave type II burst, on its low-frequency side, supports the idea that the type III bursts are emitted by electron beams accelerated at the shock wave (see Cane et al. 1981; Bougeret et al. 1998; Klassen et al. 2002; Kollhoff et al. 2021).

3.3. Origins of the forward- and reverse-drift bursts

Groups of forward- and reverse-drifting bursts are commonly found in type II bursts. Because of their characteristic pattern in the dynamic spectrum, they are called herringbone bursts. They are interpreted as electron beams accelerated at the coronal shocks that also generate the type II bands (Stewart & Magun 1980; Holman & Pesses 1983; Mann & Klassen 2005). One example is the burst group in the dynamic spectrum in Fig. 5 between 80 and 50 MHz around 15:31 UT. Similar features were reported in non-drifting type II bursts, which have been ascribed to shock waves at reconnection outflows (Aurass et al. 2002; Aurass & Mann 2004). This raises the question whether the forward-reverse-drifting bursts during the second and third group of DH type III bursts can be interpreted as herringbone bursts. One counterargument is that they are not located on the track of type II bands, as shown above; however, the track is model-dependent. Another difference from herringbones is that the burst groups on 2021 Oct. 28 comprise bursts of opposite drift in the same frequency ranges. In addition, individual well-defined bursts were found to have bandwidths comparable with their central frequencies and, therefore, larger than their start frequencies, while the statistical study of Mann & Klassen (2005) found that the average bandwidth of herringbone bursts near 50 MHz is only about 20% of their start frequency. The drift rates of the bursts on 2021 Oct. 28 are not inconsistent with herringbone bursts, but they are in the tail of the distribution reported by Mann & Klassen (2005). The same results are found when comparing with analyses of individual type II events (Carley et al. 2015; Dorovskyy et al. 2015; Morosan et al. 2019; Magdalenić et al. 2020).

This suggests a different interpretation of the second and third group of DH type III bursts than the acceleration of the radio-emitting electron beams at the coronal shock wave. The release of particles from a coronal trap through magnetic reconnection with ambient open magnetic field lines is such an alternative. It will allow previously confined electrons to escape simultaneously to the high and low corona along the newly-formed open and closed field lines. These escaping electrons would emit the forward-and reverse-drifting radio bursts. This scenario will be discussed in the following subsection.

3.4. Cartoon scenario of the radio and X-ray features

The standard 2D cartoon in Fig. 13 presents a possible scenario of the events in the solar corona. Regions depicted in red show
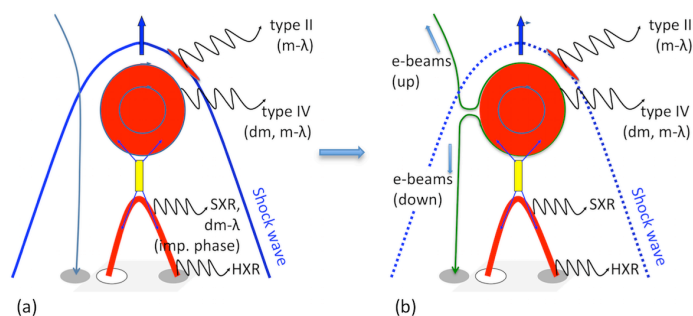

Fig. 13. Cartoon scenario of an erupting flox rope, a shock wave draped around, and suggested radio and X-ray sources (SXR = soft X-rays, HXR = hard X-rays): (*a*) shows the configuration with a neighbouring open field line, (*b*) the configuration after reconnection between the flux rope and the open field line. This enables the release of electrons that had previously been confined in the flux rope, as beams travelling upward and downward from the reconnection site.

the radio sources, namely, the cross-section of the rising flux rope (circle) and loops forming underneath. In this scenario, the impulsive emission at decimetre-wavelengths is coming from the loops in the low corona and is closely related to the hard X-rays from electrons precipitated into the two chromospheric footpoints. The soft X-rays also come from the loop, whereas radio bursts at metre-wavelengths (type *J* bursts) may come from the flux rope. The possible acceleration region is in the plasma sheet drawn as a yellow rectangle between the loops and the flux rope. The type II source, initially at metre wavelengths, is assumed to be a localised (quasi-perpendicular) region on the shock wave draped around the rising flux rope. The location of the X-ray sources and their orientation are consistent with the STIX observations and with the direction of the eruptive filament shown in the SDO/AIA images. The coronal wave seen by SDO/AIA may be the low coronal trace of the shock wave (Warmuth 2015).

The non-thermal electron populations emitting the type IV continuum are thought to be trapped. This is consistent with the low-frequency limit of the continuum. The hardening of the hard X-ray and microwave spectra corroborates this interpretation. One cause of hardening HXR bremsstrahlung and microwave gyrosynchtron spectra is the depletion of the low-energy spectrum of the radiating electrons by energy losses or scattering in Coulomb collisions (Melrose & Brown 1976; Bruggmann et al. 1994; Melnikov et al. 2002). The continuous spectral hardening has been found in HXR bursts of particularly long duration ("gradual" HXR bursts; Cliver et al. 1986; Saldanha et al. 2008). Kiplinger (1995), Saldanha et al. (2008) and Grayson et al. (2009) found bursts with spectral hardening to accompany strong SEP events. The hardening of the electron spectrum accounts for both the HXR and the microwave observations in the 2021 Oct. 28 event.

The rise of the flux rope leads to the dilution of the confined plasma and to the drift of the type IV emission to lower frequencies. As the acceleration region rises, too, fewer and fewer electrons are precipitated into the chromospheric footpoints of the loop, and the HXR emission gradually ceases, as does the microwave emission. The microwave source morphology observed by EOVSA in the previous ground-level event, on 2017 Sep. 10 (Gary et al. 2018), supports the scenario depicted in Fig. 13. It is also consistent with metre-wave imaging of gyrosynchrotron sources of type IV emission reported

in the literature. Maia et al. (2007), Démoulin et al. (2012), and Carley et al. (2017) analysed gyro-synchrotron emission from cm-to-m-wavelengths during the 2001 Apr. 15 and 2014 Sep. 01 events, which occurred near the western and slightly behind the eastern solar limb, respectively, as seen from the Earth. Both events produced relativistic protons detected on Earth (Bieber et al. 2004) or through their pion-decay gamma-ray emission (Pesce-Rollins et al. 2015). The evolution of the radio source could be compared with the white-light CMEs and was shown to undergo a gradual expansion and outward motion similar to the CMEs. Démoulin et al. (2012) located the radio source in the flux rope, which forms the cavity of the white-light CME structure. Similar evidence for gyro-synchrotron emission from expanding CME-structures was found by Bastian et al. (2001), Bain et al. (2014) and Sasikumar Raja et al. (2014) in other events. Dauphin et al. (2006) studied the 2003 Nov. 03 event, where both the gyro-synchrotron emission and a type II burst on its low-frequency side could be imaged. They found the type II source well above the gyro-synchrotron source. These observations support the localisation of the gyro-synchrotron emission in the expanding flux rope in the cartoon of Fig. 13, and of the type II source on the shock surface that is draped around. A more sophisticated analysis of the location of radio sources in an erupting magnetic field configuration inferred from photospheric measurements is presented by Carley et al. (2016).

The shock wave draped around the rising flux rope likely accelerates the first group of DH type III bursts as it intersects open coronal field lines. It may continue to accelerate particles as its flank travels through the corona, eventually reaching open field lines in the western solar hemisphere that are connected to the Earth (Papaioannou et al. 2022). In this scenario the type III bursts in the second and third group are also accelerated by the shock wave. The sources would then have to shift westward in the course of the event. However, unlike in the first DH type III group, these bursts start at higher frequencies than the signatures of type II emission in the Wind/WAVES spectrogram and the modelled type II tracks. This fact does not support the acceleration at the type II shock. We therefore consider an alternative scenario in the following, where the electron beams come from the erupting magnetic flux rope.

While expanding into the corona, the closed magnetic field structures will encounter (sooner or later) the open magnetic field lines rooted at the periphery of the active region and may reconnect with them. In the 2D cartoon, the open and closed field lines have opposite orientation before the reconnection, but this is not required in a realistic 3D configuration (Masson et al. 2019). The groups of forward- and reverse-drift bursts observed at metre-wavelengths during the second and third group of DH type III bursts are located within the yellow rectangles in Fig. 12; namely, between the suggested tracks of the type IV emission at high frequencies and type II emission at low frequencies. As depicted in the right panel of Fig. 13, reconnection of the rising flux rope with ambient open magnetic field lines enables the release of previously confined non-thermal electrons, both upward and downward. While propagating out of the trap these non-thermal electrons will form beams that emit the forward-drifting and the reverse-drifting bursts, respectively. Local acceleration during the reconnection process could also contribute to this process. This scenario is similar to the interpretation of late metre-wave type III emission in the eruptive event discussed by Salas-Matamoros et al. (2016). The start frequencies of the bursts may scatter, depending on where the reconnection occurs, but they are expected to lie between the low-frequency edge of the continuum and the type II burst.

3.5. Relationship with relativistic electrons and protons detected near and at Earth

The broad release window of the first relativistic electrons observed at L1 and the first relativistic protons at the Earth around 15:40 UT (15:35–15:47 UT, see Sect. 2.1; 500 s were added to enable comparison with electromagnetic waves observed at 1 AU) is consistent with a common release with the electrons in the third group of DH type III bursts. Such onset delays on the order of 10 min are typical of GLEs (e.g., Reames 2009; Aschwanden 2012), although the initial proton release of the strongest GLE observed in the space age occurred in the impulsive flare phase (McCracken et al. 2008; Masson et al. 2009). This difference can be understood by the identification of two successive releases (Moraal & McCracken 2012), first producing a strongly anisotropic population that tends to be missed by many neutron monitors because of their asymptotic directions, followed by a second, much less anisotropic and more slowly-evolving population that is observed by all neutron monitors with suitable cutoff rigidities. In the light of this distinction, the impulsive component of the GLE of 2021 Oct. 28 would probably have been missed and only the later one would have been observed. The missed observation of the impulsive component is consistent with the unfavourable location of the parent activity near the central meridian (McCracken et al. 2012).

One physical reason for delays may be the magnetic connection between the Sun and the Earth at the time of the GLE. Many GLEs occur while the parent active region is far (several tens of degrees in heliolongitude) from the footpoint on the solar wind source surface of the nominal Parker spiral through the Earth (e.g., Belov et al. 2010). If the relativistic particles were accelerated at a spatially extended coronal shock wave driven by a CME, one could understand onset delays as the time needed for the shock to intercept the Earth-connected magnetic field line. This interpretation has been used in connection with the observation of EUV waves in the parent eruptive events (see Rouillard et al. 2012; Pesce-Rollins et al. 2022, and discussions in Posner et al. 1997; Krucker et al. 1999; Lario et al. 2014; Miteva et al. 2014; Richardson et al. 2014). Because of the well-developed EUV wave, the 2021 Oct. 28 GLE could be a prime example for this. Papaioannou et al. (2022) report that the EUV wave arrives at open coronal field lines in the western solar hemisphere that are nominally connected to the Earth at 15:39 UT on 2021 Oct. 28, namely, at the solar release time of the first relativistic protons.

An obvious strength of this interpretation is that the magnetic connection to the Earth can be explained with a standard configuration of the interplanetary magnetic field and that the observed late release of relativistic particles onto the Earth-connected magnetic field lines is consistent with the timing of the EUV wave. But the interpretation also raises several questions, in particular regarding: why the angular distribution of relativistic protons at Earth is only weakly anisotropic if it is the case that the particles escape to open field lines in the western solar hemisphere and then travel directly to Earth. This argument was raised earlier in the discussion of electron events from the eastern solar hemisphere that were associated with EUV waves travelling westward (Miteva et al. 2014). An enhanced level of pitch-angle scattering is an obvious explanation, but it would be necessary to understand why this would occur in this specific case, whilst GLEs that clearly come from activity at well-connected longitudes are anisotropic in their early phases (McCracken et al. 2012). The scenario needs additional ingredients (e.g., perpendicular transport) to explain the observations,

and would therefore lose its attractiveness in offering a physically simple solution of the connectivity issue.

Another question considers why the association of the type II emission with the acceleration and escape of electrons in and from the corona, as witnessed by the type III bursts, is so loose in this GLE. The evidence that type III-emitting electron beams are accelerated at the coronal type II shock is strong only with respect to the first group of type III bursts. In the second, and especially the third type III group which occurs at the inferred time of release of the first relativistic protons to the Earth, the type III bursts start at higher frequencies than the observed type II emission and also at higher frequencies than the model type II burst that connects the metre-wave and potential decametre-wave signatures of type II bands. This scenario is more consistent with a particle release between the type II shock and the parent active region.

In addition to the above questions, the hypothesis that the Earth is connected to the Sun by a Parker spiral is debatable. Virtually all GLEs occur when the interplanetary magnetic field is in a strongly disturbed state (Masson et al. 2012). The perturbed structure can be understood as the cumulative effect of CMEs released earlier by the parent active region of the GLE. It is indeed typical of flares associated with GLEs that they occur after several days of eruptive activity in their active region. The 2021 Oct. 28 GLE is also of this type: two flares of class M and 15 of class C were reported by the NOAA Space Weather Prediction Center[11] between Oct. 27 and the GLE, and the direction of the interplanetary magnetic field measured at Wind and ACE was strongly variable before and during the GLE. This strong variability suggests that during GLEs, magnetic connections are different from the standard stationary and spherically symmetric solar wind model. The inference from the Parker-spiral geometry that the accelerator must be near the open coronal field lines in the active regions of the western solar hemisphere on 2021 Oct. 28 may be unrealistic.

The radio observations on 2021 Oct. 28 suggest the idea that the forward- and reverse-drifting bursts signal the release of electrons confined in the rising magnetic flux rope of the CME, as the magnetic structure reconnects with neighbouring open magnetic field lines. If the relativistic protons and electrons eventually observed at the Earth and L1 were accelerated together with the radio-emitting electrons in the corona, and initially confined in the flux rope, then they would escape together with the radio-emitting electrons. The process has been discussed, along with detailed numerical MHD simulations, by Masson and co-authors (Masson et al. 2013, 2019), who showed that particles confined within the CME can be released into an angular range comparable with the width of the CME.

The partial trapping of relativistic protons in coronal magnetic fields, be it in the loops at low altitudes or in the flux rope rising above, also provides a scenario to explain long-duration gamma-ray emission ascribed to pion-decay photons (e.g., Share et al. 2018; Ajello et al. 2021). The 2021 Oct. 28 GLE was indeed accompanied by a long-duration gamma-ray event observed by Fermi/LAT (Pesce Rollins, priv. comm.[12]). If relativistic protons can be partially trapped in either the loops forming in the low corona or the rising flux rope and leak out when the trapping configuration reconnects with ambient open magnetic field lines, the protons emitting gamma-rays at the Sun and those detected in space could have a common ori-

gin, whilst providing little, if any, correlation between the numbers. This would be in line with the poor correlation actually detected between the proton numbers inferred from Fermi/LAT gamma-ray observations and from measurements near 1 AU (de Nolfo et al. 2019). The trapping scenario was advocated by Mandzhavidze & Ramaty (1992) who showed its viability in magnetic fields with a high mirror ratio (>10) and ambient electron densities below some $10^{17}\,\mathrm{m}^{-3}$. This density is consistent with flare loops in the corona. The question of scattering into the loss cone by wave-particle interactions is not addressed, but we note that in the terrestrial radiation belts protons at hundreds of MeV can be trapped for several months. The scenario is an alternative to the widely advocated idea that the primary protons or alpha-particles are accelerated at the CME-driven shock as it travels outwards, sometimes to several tens of solar radii and stream back to the Sun. It responds to the suspected (Klein et al. 2018; Hudson 2018; Klein 2021b) and recently demonstrated (Hutchinson et al. 2022) difficulty of shock-accelerated protons to travel back to the Sun against magnetic mirroring.

The strength of this trap-plus-reconnection interpretation is its direct relationship to the observed radio spectrum of the 2021 Oct. 28 event. A major weakness is that it can only rely on modelling results and the observation of a somehow disturbed coronal and interplanetary magnetic field structure to explain how particles get access to Earth-connected interplanetary magnetic field lines. A decisive observational hint would be the location of the metre-wave radio emissions: in the scenario where the shock accelerates escaping electrons and protons near the footpoint of the nominal Parker spiral in the western hemisphere, we would expect the radio sources to be there as well. In the trap-plus-reconnection model, the radio sources could remain in the vicinity of the parent active region. The absence of metre-wave imaging observations during the 2021 Oct. 28 GLE leaves this issue open. However, it may be possible to use multi-spacecraft observations with radio spectrographs (Wind, Solar Orbiter, STEREO A, Parker Solar Probe) to constrain the location of the type III sources in the interplanetary space and see whether the late type III bursts come from near the western limb, as predicted by the shock-acceleration scenario, or from near disk centre, as predicted by the trap-plus-reconnection scenario.

---

[11] https://www.solarmonitor.org/
[12] See the quicklook plot at https://hesperia.gsfc.nasa.gov/fermi/lat/qlook/max_likelihood

References

Ajello, M., Baldini, L., Bastieri, D., et al. 2021, ApJS, 252, 13
Aschwanden, M. J. 1987, Sol. Phys., 111, 113
Aschwanden, M. J. 2002, Space Sci. Rev., 101, 1
Aschwanden, M. J. 2012, Space Sci. Rev., 171, 3
Aurass, H., & Mann, G. 2004, ApJ, 615, 526
Aurass, H., Vršnak, B., & Mann, G. 2002, A&A, 384, 273
Aurass, H., Klein, K., Zlotnik, E. Y., & Zaitsev, V. V. 2003, A&A, 410, 1001
Bain, H. M., Krucker, S., Saint-Hilaire, P., & Raftery, C. L. 2014, ApJ, 782, 43
Bastian, T. S., Benz, A. O., & Gary, D. E. 1998, ARA&A, 36, 131
Bastian, T. S., Pick, M., Kerdraon, A., Maia, D., & Vourlidas, A. 2001, ApJ, 558, L65
Belov, A. V., Eroshenko, E. A., Kryakunova, O. N., Kurt, V. G., & Yanke, V. G. 2010, Geomagnetism and Aeronomy, 50, 21
Benz, A. O., Monstein, C., Meyer, H., et al. 2009, Earth Moon Planets, 104, 277
Benz, A. O., Battaglia, M., & Vilmer, N. 2011, Sol. Phys., 273, 363
Bieber, J., Evenson, P., Dröge, W., et al. 2004, ApJ, 601, L103
Bougeret, J.-L., Kaiser, M. L., Kellogg, P. J., et al. 1995, Space Sci. Rev., 71, 231
Bougeret, J.-L., Zarka, P., Caroubalos, C., et al. 1998, Geophys. Res. Lett., 25, 2513
Bougeret, J. L., Goetz, K., Kaiser, M. L., et al. 2008, Space Sci. Rev., 136, 487
Brueckner, G. E., Howard, R. A., Koomen, M. J., et al. 1995, Sol. Phys., 162, 357
Bruggmann, G., Vilmer, N., Klein, K.-L., & Kane, S. R. 1994, Sol. Phys., 149, 171
Bruno, A., Bazilevskaya, G. A., Boezio, M., et al. 2018, ApJ, 862, 97
Bütikofer, R. 2018, in Solar Particle Radiation Storms Forecasting and Analysis, eds. O. E. Malandraki, & N. B. Crosby, 444, 95
Buttighoffer, A. 1998, A&A, 335, 295
Cairns, I. H. 2011, in The Sun, the Solar Wind, and the Heliosphere, eds. M. P. Miralles, & J. Sánchez Almeida, 4, 267
Cane, H. V., Stone, R. G., Fainberg, J., et al. 1981, Geophys. Res. Lett., 8, 1285
Cargill, P. J., Vlahos, L., Baumann, G., Drake, J. F., & Nordlund, Å. 2012, Space Sci. Rev., 173, 223
Carley, E. P., Reid, H., Vilmer, N., & Gallagher, P. T. 2015, A&A, 581, A100
Carley, E. P., Vilmer, N., & Gallagher, P. T. 2016, ApJ, 833, 87
Carley, E. P., Vilmer, N., Simões, P. J. A., & Fearraigh, Ó. B. 2017, A&A, 608, A137
Carley, E. P., Vilmer, N., & Vourlidas, A. 2020, Front. in Astron. Space Sci., 7, 79
Chupp, E. L., & Ryan, J. M. 2009, Res. Astron., 9, 11
Cliver, E. W., Dennis, B. R., Kiplinger, A. L., et al. 1986, ApJ, 305, 920
Dauphin, C., Vilmer, N., & Krucker, S. 2006, A&A, 455, 339
de Nolfo, G. A., Bruno, A., Ryan, J. M., et al. 2019, ApJ, 879, 90
Démoulin, P., Vourlidas, A., Pick, M., & Bouteille, A. 2012, ApJ, 750, 147
Desai, M., & Giacalone, J. 2016, Liv. Rev. Sol. Phys., 13, 3
Dorovskyy, V. V., Melnik, V. N., Konovalenko, A. A., et al. 2015, Sol. Phys., 290, 2031
Ergun, R. E., Larson, D., Lin, R. P., et al. 1998, ApJ, 503, 435
Fletcher, L., Dennis, B. R., Hudson, H. S., et al. 2011, Space Sci. Rev., 159, 19
Gary, D. E., Chen, B., Dennis, B. R., et al. 2018, ApJ, 863, 83
Gopalswamy, N., Xie, H., Yashiro, S., et al. 2012, Space Sci. Rev., 171, 23
Grayson, J. A., Krucker, S., & Lin, R. P. 2009, ApJ, 707, 1588
Hamini, A., Auxepaules, G., Birée, L., et al. 2021, J. Spa. Weather Spa. Clim., 11, 57
Hannah, I. G., Hudson, H. S., Battaglia, M., et al. 2011, Space Sci. Rev., 159, 263
Hoang, S., Dulk, G., & Leblanc, Y. 1994, A&A, 289, 957
Högbom, J. A. 1974, A&AS, 15, 417
Holman, G. D., & Pesses, M. E. 1983, ApJ, 267, 837
Holman, G. D., Aschwanden, M. J., Aurass, H., et al. 2011, Space Sci. Rev., 159, 107
Hudson, H. S. 2018, in Space Weather of the Heliosphere: Processes and Forecasts, eds. C. Foullon, & O. E. Malandraki, IAU Symp., 335, 49
Hutchinson, A., Dalla, S., Laitinen, T., et al. 2022, A&A, 658, A23
Huttunen-Heikinmaa, K., Valtonen, E., & Laitinen, T. 2005, A&A, 442, 673
Kiplinger, A. L. 1995, ApJ, 453, 973
Klassen, A., Bothmer, V., Mann, G., et al. 2002, A&A, 385, 1078
Klein, K.-L. 2021a, Front. Astron. Space Sci., 7, 105
Klein, K.-L. 2021b, Front. Astron. Space Sci., 7, 93
Klein, K.-L., & Dalla, S. 2017, Space Sci. Rev., 212, 1107
Klein, K. L., Tziotziou, K., Zucca, P., et al. 2018, in Solar Particle Radiation Storms Forecasting and Analysis, eds. O. E. Malandraki, & N. B. Crosby, Astrophys. Space Sci. Lib., 444, 133
Kliem, B., Karlický, M., & Benz, A. O. 2000, A&A, 360, 715
Kollhoff, A., Kouloumvakos, A., Lario, D., et al. 2021, A&A, 656, A20
Koutchmy, S. 1994, Adv. Space Res., 14, 29
Krucker, S., Larson, D. E., Lin, R. P., & Thompson, B. J. 1999, ApJ, 519, 864
Krucker, S., Hurford, G. J., Grimm, O., et al. 2020, A&A, 642, A15
Lario, D., Raouafi, N. E., Kwon, R.-Y., et al. 2014, ApJ, 797, 8
Lemen, J. R., Title, A. M., Akin, D. J., et al. 2012, Sol. Phys., 275, 17
Lopate, C. 2006, in Solar Eruptions and Energetic Particles. eds. N. Gopalswamy, R. Mewaldt, & J. Torsti, AGU Monograph (Washington DC: American Geophysical Union), 165, 283
Magdalenić, J., Marqué, C., Fallows, R. A., et al. 2020, ApJ, 897, L15
Maia, D. J. F., Gama, R., Mercier, C., et al. 2007, ApJ, 660, 874
Mandzhavidze, N., & Ramaty, R. 1992, ApJ, 396, L111
Mann, G., & Klassen, A. 2005, A&A, 441, 319
Mann, G., Melnik, V. N., Rucker, H. O., Konovalenko, A. A., & Brazhenko, A. I. 2018, A&A, 609, A41
Mann, G., Vocks, C., Warmuth, A., et al. 2022, A&A, 660, A71
Massa, P., Battaglia, A. F., Volpara, A., et al. 2022, ArXiv e-prints [arXiv:2202.09334]
Masson, S., Klein, K.-L., Bütikofer, R., et al. 2009, Sol. Phys., 257, 305
Masson, S., Démoulin, P., Dasso, S., & Klein, K.-L. 2012, A&A, 538, A32
Masson, S., Antiochos, S. K., & DeVore, C. R. 2013, ApJ, 771, 82
Masson, S., Antiochos, S. K., & DeVore, C. R. 2019, ApJ, 884, 143
McCracken, K. G., Moraal, H., & Stoker, P. H. 2008, J. Geophys. Res., 113, 12101
McCracken, K. G., Moraal, H., & Shea, M. A. 2012, ApJ, 761, 101
Melnikov, V. F., Shibasaki, K., & Reznikova, V. E. 2002, ApJ, 580, L185
Melnikov, V. F., Gary, D. E., & Nita, G. M. 2008, Sol. Phys., 253, 43
Melrose, D. B., & Brown, J. C. 1976, MNRAS, 176, 15
Miteva, R., Klein, K.-L., Kienreich, I., et al. 2014, Sol. Phys., 289, 2601
Moraal, H., & McCracken, K. G. 2012, Space Sci. Rev., 171, 85
Morosan, D. E., Carley, E. P., Hayes, L. A., et al. 2019, Nat. Astron., 3, 452
Müller, D., Nicula, B., Felix, S., et al. 2017, A&A, 606, A10
Müller, D., St. Cyr, O. C., Zouganelis, I., et al. 2020, A&A, 642, A1
Müller-Mellin, R., Kunow, H., Fleissner, V., et al. 1995, Sol. Phys., 162, 483
Newkirk, G., Jr. 1967, ARA&A, 5, 213
Nindos, A., Aurass, H., Klein, K.-L., & Trottet, G. 2008, Sol. Phys., 253, 3
Papaioannou, A., Kouloumvakos, A., Mishev, A., et al. 2022, A&A, 660, L5
Pesce-Rollins, M., Omodei, N., Petrosian, V., et al. 2015, ApJ, 805, L15
Pesce-Rollins, M., Omodei, N., Krucker, S., et al. 2022, ApJ, 929, 172
Petrosian, V. 2012, Space Sci. Rev., 173, 535
Pick, M. 1986, Sol. Phys., 104, 19
Posner, A., Bothmer, V., Kunow, H., et al. 1997, in Correlated Phenomena at the Sun, in the Heliosphere and in Geospace, ed. A. Wilson, ESA Special Publ., 415, 377
Reames, D. V. 2009, ApJ, 693, 812
Reiner, M. J., & MacDowall, R. J. 2015, Sol. Phys., 290, 2975
Richardson, I. G., von Rosenvinge, T. T., Cane, H. V., et al. 2014, Sol. Phys., 289, 3059
Rouillard, A. P., Sheeley, N. R., Tylka, A., et al. 2012, ApJ, 752, 44
Saint-Hilaire, P., Vilmer, N., & Kerdraon, A. 2013, ApJ, 762, 60
Salas-Matamoros, C., Klein, K.-L., & Rouillard, A. P. 2016, A&A, 590, A135
Saldanha, R., Krucker, S., & Lin, R. P. 2008, ApJ, 673, 1169
Sasikumar Raja, K., Ramesh, R., Hariharan, K., Kathiravan, C., & Wang, T. J. 2014, ApJ, 796, 56
Seaton, D. B., Berghmans, D., Nicula, B., et al. 2013, Sol. Phys., 286, 43
Share, G. H., Murphy, R. J., White, S. M., et al. 2018, ApJ, 869, 182
Sinclair Reid, H. A., & Ratcliffe, H. 2014, Res. Astron. Astrophys., 14, 773
Smerd, S. F., Sheridan, K. V., & Stewart, R. T. 1975, ApJ, 16, 23
Stewart, R. T., & Magun, A. 1980, PASA, 4, 53
Vainio, R., & Afanasiev, A. 2018, in Solar Particle Radiation Storms Forecasting and Analysis, eds. O. E. Malandraki, & N. B. Crosby, Astrophys. Space Sci. Lib., 444, 45
Vršnak, B., & Cliver, E. W. 2008, Sol. Phys., 253, 215
Vršnak, B., Aurass, H., Magdalenić, J., & Gopalswamy, N. 2001, A&A, 377, 321
Warmuth, A. 2015, Liv. Rev. Sol. Phys., 12, 3
Warmuth, A., & Mann, G. 2005, A&A, 435, 1123
Warmuth, A., Önel, H., Mann, G., et al. 2020, Sol. Phys., 295, 1
Zucca, P., Carley, E. P., McCauley, J., et al. 2012, Sol. Phys., 280, 591
Zucca, P., Carley, E. P., Bloomfield, D. S., & Gallagher, P. T. 2014, A&A, 564, A47

Appendix A: Simple model of the type II burst trajectory in a hydrostatic corona
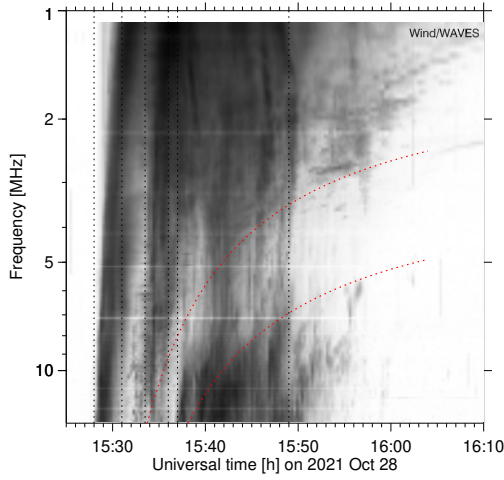

Fig. A.1. Dynamic spectrogram from 14 to 1 MHz with overlaid tracks (dashed red curves) of the fundamental and harmonic bands of a model type II burst. See text for details.

The radio spectrum of the 2021 Oct 28 event shows well-defined signatures of type II emission at metre-wavelengths (∼300-25 MHz; see Sect. 2.3.4) and fragments of possible type II emission at decametre-to-hectometre wavelengths (Wind/WAVES), henceforth referred to as DH-λ. For example the spectrogram in Fig. A.1 shows a narrow drifting band between about 16:02 and 16:10 UT at frequencies just above 2 MHz, and others at slightly higher frequencies (15:51-15:56 UT) and in the 1-2 MHz range (starting near 15:59 UT). These fragments are scattered over too broad a frequency range to be considered as part of a single type II band. The entire emission at frequencies below 2 MHz that becomes visible since 15:50 UT, after the type III bursts, could be of type II.

In order to explore possible links between the features at m-λ and DH-λ, we use a spherically symmetric isothermal hydrostatic model of the corona. The electron plasma frequency as a function of heliocentric distance, r, is:

$$\nu_{\mathrm{pe}}(r) = \nu_{\mathrm{pe}}(R_\odot) \exp\left(-\frac{R_\odot}{2H_\odot}\left(1 - \frac{R_\odot}{r}\right)\right) , \qquad (A.1)$$

where

$$H_\odot = 50.1 \cdot 10^6 \frac{T}{1\,\mathrm{MK}} \ [\mathrm{m}]$$

is the scale height for an isothermal plasma with temperature, T, and mean molecular weight of 0.6. This represents Newkirk's density model (Newkirk 1967) when $T = 1.40 \cdot 10^6$ K. In the vicinity of the heliocentric distance, r_0, the plasma frequency profile has an exponential decay. Thus, the local logarithmic derivative of the frequency-time trajectory of the type II burst in the vicinity of r_0 is:

$$\frac{d}{dt}\ln\nu = V\cos\theta \frac{d}{dr}\ln\nu = -\frac{V\cos\theta}{2H_\odot}\left(\frac{R_\odot}{r_0}\right)^2 . \qquad (A.2)$$

Table A.1. Input parameters and results of the hydrostatic model of type II emission connecting spectral features at metre- and decametre-wavelengths.

Input:	Time [UT]	Frequency [MHz]	Log. drift rate [s^{-1}]	
m-λ	15:28:40	89.7	$-9.27 \cdot 10^{-3}$	
DH-λ	16:05:37	2.4	$-2.20 \cdot 10^{-4}$	
Results:	r [$R_\odot$]	V [km s^{-1}]	θ	$n_e(R_\odot)$ [m^{-3}]
m-λ	1.19	2586	44.6°	$4.82 \cdot 10^{14}$
DH-λ	9.12		5.2°	

V is the speed and θ the angle with respect to the radial direction at which the exciter propagates through the corona. This relationship is independent of whether the radio emission is at the fundamental or the harmonic.

We measured the central frequency of the low-frequency harmonic type II splitband and its logarithmic drift rate in the ORFEES spectrum, and of the narrow band 16:02-16:10 UT just above 2 MHz in the Wind/WAVES spectrum. This band is selected with the aim of obtaining a track which represents the type II band at the highest frequencies consistent with the observations. The aim is also to be as close as possible to the metre-wave bursts with forward and reverse frequency drift, so that we may explore whether they can be related with the type II shock (or not). Under the assumption that the exciter of the type II burst travels along a straight line, the ratio of the central frequencies, the times when the type II burst is observed at these frequencies and the logarithmic drift rates determine the spatial profile of the electron plasma frequency. The drift rates and central frequencies are inferred from linear fits to the ln(frequency) versus the time trajectory of the type II bands in the two spectral ranges. The presumed DH type II band can be either fundamental or harmonic emission. The observed parameters listed in the upper table of Table A.1 use the assumption that it is fundamental. The derived heliocentric distances, exciter speed and propagation angles, and the electron density at the coronal base are those quoted in the lower table. No solution is found if the DH-λ emission is supposed to be at the harmonic. The inferred exciter speed is much higher than the projected speed of the CME front in the SoHO/LASCO observations. The base density is slightly higher than Newkirk's value in the solar minimum equatorial corona (Newkirk 1967, Table I) and eclipse observations analysed by Koutchmy (1994).

The resulting fundamental and harmonic type II lanes are superposed by dashed red lines on the spectrogram in Fig. A.1. The modelled fundamental band is close to the high-frequency limit of diffuse emission that becomes visible in the spectrum after the end of DH type III bursts near 15:50 UT. However, the model is clearly oversimplified, since we cannot expect to describe the corona by a hydrostatic model out to more than 9 $R_\odot$. We did not seek to refine the model, however, because this would introduce more parameters. The modelled type II bands are mainly intended to guide the eye in the discussion of relationships between different types of radio emission identified in this event.